ACCSCIENCE PUBLISHING

International Journal of Bioprinting

RESEARCH ARTICLE

Immunomodulatory 3D-printed hydroxyapatite/tricalcium phosphate/polycaprolactone scaffolds promote bone regeneration via macrophage polarization

Hao Tang[1†], Guangquan Zhao[1†], Yuanhao Lv[1†], Qianyu Xie[1], Jiaxiang Song[1], Shuai Huang[3*], Weikang Xu[2*], and Qingde Wa[1*]

[1]Department of Orthopedic Surgery, The Second Affiliate Hospital of Zunyi Medical University, Zunyi, Guizhou, China

[2]Medical Materials and Engineering Research Laboratory, Institute of Biological and Medical Engineering, Guangdong Academy of Sciences, Guangzhou, China

[3]Department of Orthopaedic Surgery, The First People's Hospital of Foshan, School of Medicine, Southern University of Science and Technology, Foshan, Guangdong, China

[†]*These authors contributed equally to this work.*

***Corresponding authors:**
Shuai Huang
(huangshuai316@163.com)
Weikang Xu
(759200816@qq.com)
Qingde Wa
(wqd887zsy@126.com)

Citation: Tang H, Zhao G, Lv Y, *et al*. Immunomodulatory 3D-printed hydroxyapatite/tricalcium phosphate/polycaprolactone scaffolds promote bone regeneration via macrophage polarization. *Int J Bioprint*. 2026:12(2):026060049. doi: 10.36922/IJB026060049

Received: February 4, 2026

Revised: March 22, 2026

Accepted: March 30, 2026

Published online: April 22, 2026

(This article belongs to the *Special Issue: 3D Printing and Bioprinting Technologies for Bone Repair and Regeneration*)

Abstract

Excessive inflammation remains a significant impediment to the regeneration of critical-sized bone defects, where the local immune microenvironment plays a crucial role in osteogenesis. However, most bone scaffolds primarily emphasize mechanical support and osteoconductivity, while their immunomodulatory potential remains largely unexplored. In this study, we designed and fabricated three-dimensional–printed hydroxyapatite/β-tricalcium phosphate/polycaprolactone (HTP) composite scaffolds to regulate macrophage polarization and promote bone regeneration. The HTP scaffolds demonstrated exceptional structural integrity and mechanical strength, facilitating the adhesion, proliferation, and osteogenic differentiation of bone marrow-derived mesenchymal stem cells. Notably, the HTP scaffolds effectively modulated the immune microenvironment by inhibiting the polarization of pro-inflammatory M1 macrophages and promoting their transition toward the regenerative M2 phenotype. This immunomodulatory effect further enhanced osteogenic factor secretion, establishing a correlation between immunoregulation and osteogenesis. In a rat calvarial defect model, the HTP scaffolds significantly increased M2 macrophage infiltration, promoted angiogenesis, and accelerated new bone formation compared to other groups. This study demonstrates that three-dimensional–printed HTP composite scaffolds promote bone regeneration and angiogenesis by establishing a regenerative immune microenvironment, highlighting their potential as an advanced immunomodulatory platform for bone tissue engineering.

Keywords: Bone repair; Hydroxyapatite; Macrophage polarization; β-tricalcium phosphate; Three-dimensional printing

1. Introduction

Bone defects, caused by various pathological factors such as trauma, infection, tumor resection, and congenital deformities, result in the continuous loss of bone tissue. This can lead to local or widespread bone volume (BV) loss and impaired bone function, severely affecting the patient's quality of life.[1] For bone defects exceeding the "critical size," the body's self-repair capacity is limited, often resulting in non-union or functional loss.[2] Current clinical treatments include autologous bone grafting, allogeneic bone grafting, and artificial bone repair material implantation.[3] Although autologous bone grafting is considered the "gold standard" for bone defect repair because it contains viable osteogenic cells, native bone matrix, and endogenous growth factors, it is limited by insufficient donor bone supply, donor site complications, and significant surgical trauma.[4] Allogeneic bone grafting helps overcome donor bone shortage to some extent but poses risks such as immune rejection, disease transmission, and limited bone reconstruction capacity.[5] Artificial bone repair materials based on biomaterials (e.g., bioceramics and biodegradable polymers) partially address these shortcomings. However, their biological activity, immunomodulatory capacity, and mechanical properties still do not fully meet clinical needs.[6] Therefore, the development of novel bone repair scaffolds with good biocompatibility, mechanical properties, and immunomodulatory capabilities has become an important research direction in bone tissue engineering.

Polycaprolactone (PCL) is a degradable synthetic polyester that has attracted considerable attention and achieved partial clinical application due to its excellent biocompatibility, controllable degradation, superior plasticity, and processing performance, making it suitable for various fabrication methods, such as melt extrusion and three-dimensional (3D) printing.[7] PCL scaffolds provide mechanical support in weight-bearing environments, and their design can be personalized to defect sites and individual patient differences.[8] However, PCL molecular chains contain many hydrophobic -CH_2 groups, leading to poor surface hydrophilicity, which impairs cell adhesion and proliferation. Moreover, its inherent biological activity and osteoinductive capacity are weak, and its degradation rate is slow in specific applications, limiting its use in complex bone defect repairs.[9] Recent studies have focused on the construction of "organic polymer/inorganic bioceramic" composite scaffolds to optimize mechanical properties, degradation behavior, and biological activity.[10]

Hydroxyapatite (HA), a major inorganic component of natural bone, has chemical and structural similarities to bone tissue, providing excellent biocompatibility and osteoconductivity. HA promotes osteocyte adhesion, proliferation, and mineralization, which positively impacts new bone formation. However, HA is brittle, with low tensile strength and fracture toughness, making it unsuitable for complex stress environments, and its poor *in vivo* resorption can hinder bone reconstruction.[11]

Tricalcium phosphate (TCP), a commonly used degradable bioceramic, has good biocompatibility and a controllable degradation rate. It releases Ca^{2+} and PO_4^{3-} ions, providing essential minerals for bone regeneration, and its porous structure promotes fluid infiltration and cell ingrowth.[12] However, pure TCP degrades rapidly *in vivo*, causing inadequate support and incomplete bone reconstruction, with limited osteoinductive capacity.[13]

Studies have shown that combining PCL with HA, TCP, and other inorganic phases improves scaffold surface wettability, bioactivity, and cell adhesion, proliferation, and osteogenic differentiation.[13] For example, HA/PCL (HP) composite scaffolds effectively support osteoprogenitor cell adhesion and mineralization, while TCP/PCL (TP) scaffolds can adjust degradation rates and osteoconductivity by varying the ceramic content.[14,15] Furthermore, regulating the organic/inorganic phase ratio in the scaffold (e.g., 50% organic and 50% inorganic) balances mechanical properties and bioactivity, thereby improving cell proliferation and mineralization and promoting new bone formation.[16] However, most studies focus primarily on osteoconductivity and mechanical strengthening, with relatively limited research on regulating the bone immune microenvironment and achieving a synergistic "immunomodulation–osteogenic repair" effect in composite scaffolds.

Recent research in osteoimmunology has shown that bone repair is not merely a cellular process but the result of a highly integrated interaction between the immune system and bone remodeling.[17] After scaffold implantation, immune cells are the first to interact with the material, followed by protein adsorption, inflammatory cell infiltration, and foreign body reactions. The interaction between the implant material and the immune microenvironment largely determines the outcome of bone repair.[18] If the early inflammatory response is excessive or prolonged, it can lead to fibrous encapsulation, poor bone–material interface integration, or implant failure. Conversely, moderate and timely regulation of inflammation promotes the resolution of inflammation, tissue remodeling, and new bone formation.[19]

Macrophages, as key immune regulatory cells, are highly plastic and can polarize into the classical M1 phenotype (pro-inflammatory) or the alternative M2 phenotype (anti-inflammatory/repair) under different microenvironmental stimuli.[20] M1 macrophages participate in pathogen

clearance and early inflammation amplification by secreting interleukin (IL)-1β, tumor necrosis factor (TNF)-α, and inducible nitric oxide synthase (iNOS), but long-term dominance can lead to chronic inflammation and implant failure. M2 macrophages, by secreting IL-10, transforming growth factor-β, and bone morphogenetic protein (BMP)-2, inhibit inflammation, promote angiogenesis, and support bone formation, playing an indispensable role in bone regeneration.[21] Therefore, inducing an appropriate transition from M1 to M2 macrophages through scaffold design and surface modification, thereby creating an immune microenvironment favorable for osteogenesis, has become a crucial approach for improving clinical translation of bone repair materials.

Hydroxyapatite and TCP complement each other in chemical composition and degradation behavior. HA degrades slowly and has strong osteoconductivity, while TCP degrades rapidly, releasing ample Ca^{2+} and PO_4^{3-} ions, and has specific acid–base buffering capacity.[22] Introducing varying proportions of HA/TCP into a PCL scaffold can synergistically regulate its mechanical properties, surface roughness, ion release behavior, and acid–base environment, thereby influencing the adhesion, migration, and functional state of immune and osteogenic cells.[16,23] Therefore, constructing HA/TCP/PCL (HTP) composite scaffolds and systematically evaluating their immunomodulatory and bone repair capabilities is of great significance for enriching the theoretical basis of HA/TCP-based bioceramic–polymer composites and expanding their clinical applications.

In this study, 3D printing technology was employed to construct HTP composite scaffolds using PCL as the degradable organic matrix, thereby introducing a reasonable ratio of HA and TCP to improve the overall mechanical properties, surface bioactivity, degradation behavior, and ion release characteristics of the scaffold. Additionally, the physicochemical properties, mechanical performance, and *in vitro* biocompatibility of the HTP composite scaffolds were systematically evaluated, focusing on their effects on macrophage polarization, inflammatory cytokine secretion, and osteogenic cell behavior. Moreover, their immunomodulatory role in the bone immune microenvironment was investigated, and their *in vivo* bone repair effect in a calvarial defect animal model was further validated. This study aims to develop an HTP composite scaffold with both immunomodulatory and bone repair capabilities, providing new material strategies and theoretical foundations for tissue engineering repair of complex bone defects (Figure 1).

2. Materials and methods

2.1. Materials

Polycaprolactone (molecular weight = 50 kDa, particle size < 600 μm) was obtained from Polysciences Inc. (USA). HA (nanoXIM·HAp202; molecular weight = 1,004.6; d50 = 5.0 ± 1.0 μm) and TCP (nanoXIM·TCP200; molecular weight = 310.09; d50 = 5.0 ± 2.0 μm) were provided by Fluidinova (Portugal).

The ultra-pure RNA reagent kit (catalog no. CW0581S, CWBIO, Beijing, China), HiFiScript cDNA synthesis kit (catalog no. CW2569M, CWBIO, Beijing, China) , and UltraSYBR Mix (low ROX) were purchased from CWBIO (China). Alkaline phosphatase (ALP) detection kits (catalog no. E-BC-K235-S, Biotime Biotechnology Co., Ltd., Wuhan, China), bicinchoninic acid protein detection kits (catalog no. E-BC-K114-S, Biotime Biotechnology Co., Ltd., Wuhan, China) , and radioimmunoprecipitation lysis buffer were supplied by Biotime Biotechnology Co., Ltd. (China). Dulbecco's Modified Eagle Medium (DMEM), fetal bovine serum (FBS), penicillin–streptomycin solution, phosphate-buffered saline (PBS), trypsin, and Cell Counting Kit (CCK)-8 cell (catalog no. CK04, Dojindo Molecular Technologies, Kumamoto, Japan) (were purchased from Gibco (USA).

Rat bone marrow-derived mesenchymal stem cells (BMSCs) and RAW264.7 macrophages were sourced from Gibco (USA) and the American Type Culture Collection (USA), respectively. IL-10 (EM220162, BYabscience, China), IL-12 (EM220166, BYabscience, China), rabbit anti-iNOS antibody (GB11119, Servicebio, China), and rabbit anti-CD163 antibody (GB15340, Servicebio, China) were used, along with a horseradish peroxidase-conjugated goat anti-rabbit IgG secondary antibody (GB23303, Servicebio, China). Anti–BMP-2 antibody (bs-1012R, Bioss, China) and AlexaFluor488-conjugated goat anti-rabbit IgG secondary antibody (bs-1012R, Bioss, China) were used for detection. Anti-vascular endothelial growth factor (VEGF) antibody (GB15165, Servicebio, China) was also utilized.

2.2. Preparation of HTP scaffolds

Tricalcium phosphate (200 mg), HA (200 mg), and TCP (100 mg) mixed with HA (100 mg) were each dispersed by vigorous magnetic stirring and brief ultrasonication in 10 mL of dichloromethane solution (Sigma-Aldrich, USA) containing 800 mg of PCL. The mixture was thoroughly stirred and then poured into respective glass dishes, where dichloromethane was allowed to evaporate, resulting in the raw materials for TP, HP, and HTP scaffolds. These

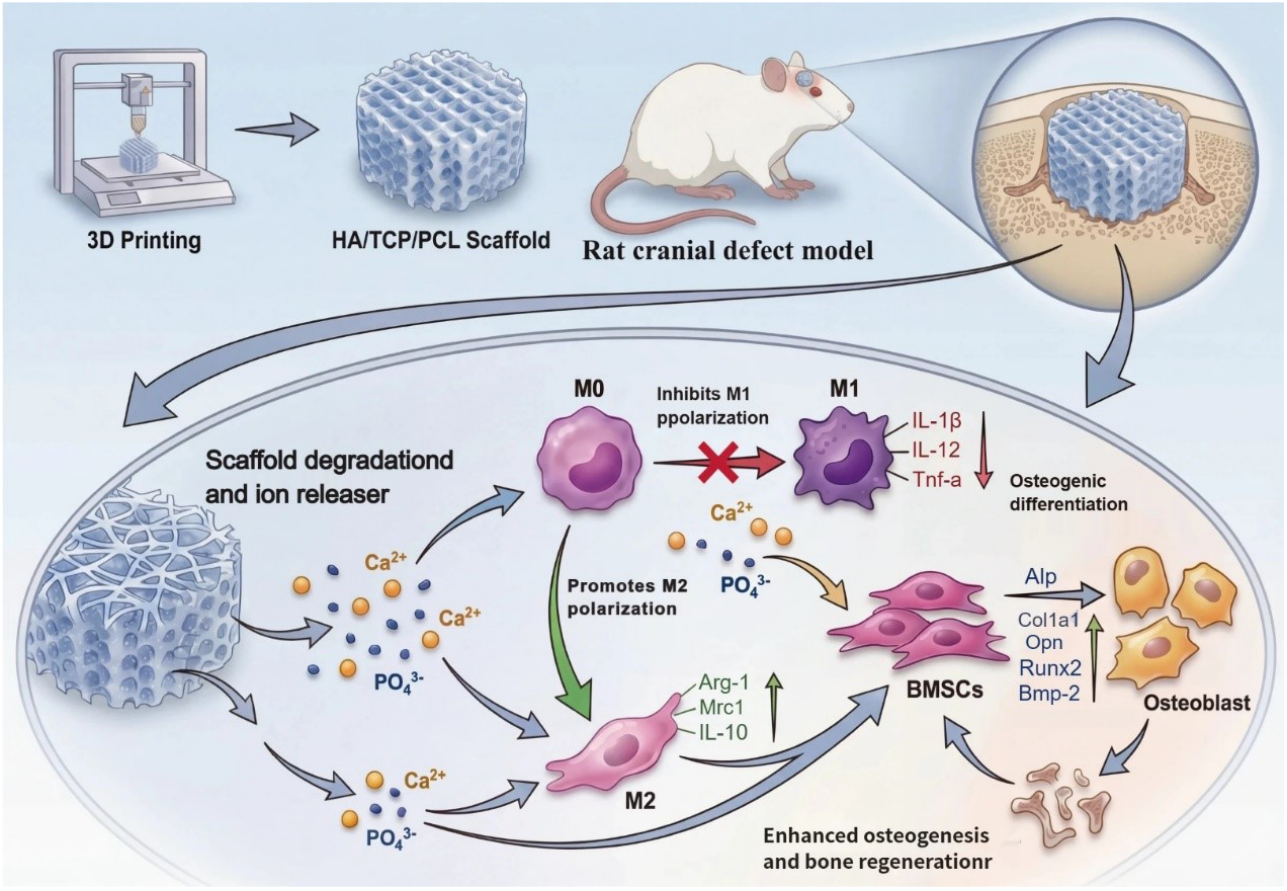

Figure 1. Schematic illustration of bone regeneration promoted by immunomodulation using 3D-printed HA/TCP/PCL composite scaffolds. HA/TCP/PCL porous scaffolds were fabricated via 3D printing and implanted into a rat calvarial critical-sized defect model. The scaffolds gradually degrade *in vivo*, releasing ions such as Ca^{2+} and PO_4^{3-}, which enhance the local microenvironment and regulate macrophage polarization. This process inhibits the polarization of pro-inflammatory M1 macrophages and their associated inflammatory cytokines (e.g., TNF-α, IL-1β, IL-12), while promoting the polarization of regenerative M2 macrophages and upregulating related markers (e.g., *Mrc1*, *Arg1*) and the anti-inflammatory cytokine IL-10, thus creating an immune microenvironment favorable for bone regeneration. This immune microenvironment further enhances the adhesion and osteogenic differentiation of bone marrow-derived mesenchymal stem cells, increasing osteogenesis-related markers (e.g., *Alp*, *Runx2*, *Opn*, *Col1a1*, and *Bmp2*), ultimately promoting enhanced osteogenesis and repair of the calvarial defect. Figure created with Adobe Illustrator 2022 in accordance with Adobe's licensing terms (https://www.adobe.com/legal/subscription-terms.html).
Abbreviations: 3D: Three-dimensional; HA: Hydroxyapatite; IL: Interleukin; PCL: Polycaprolactone; TCP: Tricalcium phosphate; TNF-α: Tumor necrosis factor α.

materials were then loaded into the feed barrel of a 3D printer (EFL-BP-6603, Suzhou Institute of Intelligent Manufacturing, China) and heated to their melting point. The nozzle diameter was set to 0.25 mm, the feed barrel temperature was set to 75 °C, and the nozzle temperature was set to 80 °C. Fiber spacing was set to 0.8 mm × 0.8 mm, print speed was set to 10 mm/s, and fiber orientation was set to 0–90°. The air pressure was set at 400 kPa, and the layer height was set to 80% of the nozzle diameter. The printed cylindrical 3D scaffolds had a diameter of 10 mm and a height of 5 mm for mechanical strength testing, and a diameter of 5 mm and a height of 1 mm for biological performance and cell-based experiments.

2.3. Surface characterization of scaffolds

2.3.1. Surface morphology analysis

The surface morphology and structure of the PCL, HP, TP, and HTP scaffolds were characterized using a high-resolution field-emission scanning electron microscope (SEM; Zeiss, Germany) and a transmission electron microscope (JEM-2100HR, JEOL, Japan). Energy-dispersive X-ray spectroscopy (Oxford Instruments [Ultim Max],UK) was then used to characterize the elemental composition and distribution on the surfaces of the

scaffolds.

2.3.2. Component analysis

Thermogravimetric analysis was performed to measure the weight loss behavior of the scaffolds. The samples were heated from room temperature to 800 °C at a rate of 10 °C/min under a nitrogen atmosphere.

2.3.3. Measurement of scaffold porosity

The samples soaked in ethanol at room temperature were labeled as M1. The samples were then dried in a densitometer (Oxford Instruments, Abingdon, UK) , and the dry mass of the scaffolds was recorded as M0. After performing ultrasonication in anhydrous ethanol using a densitometer for 10 min to remove air bubbles, the total mass of the samples was recorded as M2. After removing the samples, the remaining mass was measured as M3. The porosity of the scaffolds was calculated using the following formula:

$$P = \frac{(M_2 - M_3 - M_0)}{(M_1 - M_3)} \quad (1)$$

2.3.4. Scaffold hydrophilicity test

Ultrapure water (2 μL) was gently placed onto the surface of the sample using a microsyringe, and the droplet deposition process was recorded with a high-resolution camera (KRÜSS GmbH,Germany). The dynamic contact angle between the droplet and the scaffold surface was measured using a contact angle goniometer (KRÜSS DSA100, Hamburg, Germany).

2.3.5. Scaffold mechanical strength test

The mechanical properties of the scaffolds were analyzed using an INSTRON 345C-S testing machine (Instron, USA). At room temperature, the height of each scaffold was measured with a digital caliper, and the scaffold was placed on the testing platform. The compression speed was set to 5 mm/min, and the test was stopped when the scaffold reached 80% compressive deformation. The load values recorded during the compression phase were used to determine the compressive modulus of the scaffold. Mechanical performance was evaluated in the dry state at room temperature.

2.3.6. Ion release analysis

To evaluate the ion release behavior of the ceramic-containing scaffolds, HP, TP, and HTP scaffolds with comparable initial masses were prepared, and their initial dry weights in mg were recorded. Three replicates were included in each group. Each scaffold was immersed in 10 mL of PBS (pH 7.4) in a centrifuge tube and incubated at 37 °C under static conditions or with shaking in a thermostatic shaker. The immersion solutions were collected on days 1 and 3. Samples collected on day 1 were used to reflect early-stage ion release, whereas those collected on day 3 were used to evaluate subsequent release behavior.

Cumulative ion release was calculated as the sum of the values obtained on days 1 and 3. After each sampling, an equal volume of fresh PBS was added to maintain a constant extraction volume. The concentrations of Ca^{2+} and PO_4^{3-} in the collected solutions were measured by inductively coupled plasma optical emission spectrometry (PerkinElmer, USA). The measured values were normalized to the initial dry weight of the scaffolds and expressed as $mg \cdot L^{-1} \cdot mg^{-1}$.

2.4. Cell experiments

2.4.1. Cell culture and scaffold sterilization

Rat BMSCs and RAW264.7 cells were cultured after thawing in a constant temperature incubator (MCO-18AIC, PHCbi, Japan) at 37 °C with 5% CO_2. The complete culture medium consisted of high-glucose DMEM supplemented with 10% FBS, 100 μg/mL penicillin, and 100 μg/mL streptomycin. The medium was replaced daily or every two days, depending on the cell condition. Cell passaging was conducted when the cells reached 70–80% confluency, and only cells from passages 3 to 5 were used for subsequent experiments. Before the experiment, scaffolds were sterilized by immersion in 75% ethanol for 2 h, followed by three washes with PBS and overnight ultraviolet sterilization (Shenzhen Zhiyuan and Kejia Education Equipment Co., Ltd., China).

2.4.2. Biocompatibility evaluation of the scaffolds

The biocompatibility of the scaffolds with BMSCs was evaluated. Briefly, sterilized scaffolds were placed in 48-well plates, and BMSCs (5×10^4 cells/well) were seeded onto each scaffold. After 1, 3, and 7 days of culture, the culture medium was removed, and cell proliferation was assessed using the CCK-8 assay. Optical density values were measured using a microplate reader (TecanSpark, Austria). Cell viability was determined by live/dead cell staining, and cell morphology and distribution on the scaffold surface were observed using an inverted fluorescence microscope. After 72 h of cell adhesion and proliferation on the scaffold surface, selected cells underwent further analysis.

2.4.3. Osteogenic differentiation assays

Rat BMSCs (1×10^5 cells/well) were seeded onto sterile scaffolds in 48-well plates and incubated for 24 h to facilitate adhesion. The culture medium was then replaced with complete medium, osteogenic induction

medium (complete medium supplemented with 0.039 μg/mL dexamethasone, 50 μg/mL ascorbic acid, and 10 mM β-glycerophosphate), or macrophage-conditioned medium, refreshed every 2–3 days.

At day 7 post-induction, ALP staining was performed using commercial kits according to the manufacturer's instructions. Calcium deposition was assessed by Alizarin Red S staining at day 14. The stained cultures were imaged using a light microscope (Olympus BX53, Tokyo, Japan).

For comparative evaluation between blank controls (Con) and scaffold groups, indirect co-culture was established using Transwell inserts (with scaffolds in the upper chamber and BMSCs in the lower chamber). ALP staining was conducted at day 7, with ALP activity quantified colorimetrically using an ALP assay kit and normalized to total protein (bicinchoninic acid assay). Alizarin Red S staining at day 14 was followed by destaining with 10% cetylpyridinium chloride and measurement of absorbance at 562 nm (Tecan Spark plate reader, Männedorf, Switzerland) to quantify calcium deposition.

At days 7 and 14, cells were harvested for total RNA extraction and real-time quantitative polymerase chain reaction (qRT-PCR) analysis, with *Gapdh* used as the housekeeping gene. Relative expression of osteogenic markers—*Alp*, *Runx2*, *Opn*, *Col1a1*, and *Bmp2*—was determined. Primer sequences are listed in Table 1.

2.4.4. Macrophage polarization assessment

RAW264.7 macrophages (5×10^4 cells/well) were seeded onto scaffolds in different groups in 48-well plates, with blank controls. Total RNA was extracted from each sample on days 1 and 3 for qRT-PCR analysis. *Gapdh* served as the housekeeping gene for normalization to quantify M1 markers (e.g., IL-1β, TNF-α) and M2 markers (e.g., CD206, ARG-1). Primer sequences are provided in Table 1.

Cell-free supernatants were collected at days 1 and 3, and IL-12/IL-10 concentrations were determined using an enzyme-linked immunosorbent assay (ELISA) kit (catalog no. EK0416, Boster Biological Technology, Pleasanton, CA, USA). Absorbance was measured at 450 nm using a Tecan Spark microplate reader (Männedorf, Switzerland), with cytokine levels calculated based on standard curves.

2.4.5. Flow cytometric analysis of macrophage polarization

To further evaluate macrophage polarization at the phenotype level, flow cytometry was performed after RAW264.7 cells were cultured with different scaffolds. Sterilized Con, PCL, HP, TP, and HTP scaffolds were placed in 6-well plates, and RAW264.7 cells were seeded onto the scaffolds and cultured at 37 °C in a humidified incubator with 5% CO_2 for 24 h.

At the end of culture, the cells were collected and washed three times with PBS to obtain single-cell suspensions. The cells were then incubated with fluorescein isothiocyanate-conjugated anti-mouse CD86 antibody (cat. no. 105011, BioLegend, USA) and phycoerythrin-conjugated anti-mouse CD206 antibody (cat. no. 141706,BioLegend,USA) for 30 min on ice in the dark. After staining, the cells were washed and resuspended in PBS containing 3% FBS, followed by flow cytometric analysis. During data analysis, cell debris and doublets were excluded by sequential gating. The percentages of $CD86^+CD206^-$ cells and $CD86^-CD206^+$ cells were quantified and used to represent M1-like and M2-like macrophage populations, respectively.

2.4.6. Scaffold-mediated immunomodulation of osteogenesis

RAW264.7 cells (5×10^4 cells/well) were cultured on scaffolds or blank controls in 48-well plates for three days. Harvested supernatants were combined at a 1:1 (v/v) ratio with osteogenic medium to generate conditioned medium, which was used to induce BMSC differentiation. Downstream assessments followed the methods described

Table 1. Specific primers used for genes involved in osteogenesis and macrophage polarization

Gene	Forward primer sequence (5'–3')	Reverse primer sequence (5'–3')
Runx2	TCGGAGAGGTACCAGATGGG	AGGTGAAACTCTTGCCTCGT
Col1a1	TTCTCCTGGCAAAGACGGAC	CTCAAGGTCACGGTCACGAA
Alp	GGAGATGGTATGGGCGTCTC	GGACCTGAGCGTTGGTGTTA
Mrc1	ATGGATGTTGATGGCTACTGG	TTCTGACTCTGGACACTTGC
Arg1	TGGACAGACTAGGAATTGGCA	CCAGTCCGTCAACATCAAAACT
Tnfa	GAGGCCAAGCCCTGGTATG	CGGGCCGATTGATCTCAGC
Il1b	TACAGGCTCCGAGATGAACA	AGGCCACAGGTATTTTGTCG
Gapdh	GCCATGAGGTCCACCACCCT	AAGGTCATCCCAGAGCTG

in Section 2.4.3.

2.5. Animal experiments

Male Sprague–Dawley (SD) rats (eight weeks old; n = 66) were used to establish a bilateral calvarial defect model for *in vivo* evaluation. Two critical-sized defects were created symmetrically in each rat calvarium, and the left and right defects received scaffold implants according to predefined pairwise groupings: Con–Con, Con–PCL, Con–TP, Con–HP, Con–HTP, PCL–TP, PCL–HP, PCL–HTP, TP–HP, TP–HTP, and HP–HTP. The detailed allocation of materials to the left and right defects is summarized in Table 2.

Rats were randomly assigned to each pairwise implantation group (n = 6 per group) using a random number table. For each group, two rats were sacrificed at each time point (1, 2, and 3 months). Accordingly, each time point included n = 2 animals per group. Thus, the bilateral defects within the same animal constituted paired observations, whereas animals from different groups or time points were considered independent. Micro-computed tomography (micro-CT) and histological analyses were performed by an investigator blinded to group allocation.

2.5.1. Establishment of bilateral calvarial defects in Sprague–Dawley rats

Prior to surgery, all SD rats were fasted for 12 h and deprived of water for 8 h. Four types of scaffolds were pre-incubated in high-glucose DMEM complete medium (containing 10% serum, 100 μg/mL penicillin, and 100 μg/mL streptomycin) overnight, one day prior to surgery.

Anesthesia was induced by intraperitoneal injection of a mixture of 8% chloral hydrate and 20% urethane. Once anesthesia was achieved, the hair over the calvarial area was shaved, and the rats were fixed in the prone position on the surgical table. The surgical area was disinfected with 1% iodine tincture and covered with sterile gauze.

A 2-cm incision was made along the midline of the calvaria, and the subcutaneous and periosteal tissues were gently separated using a surgical scalpel to expose the bilateral parietal bones, occipital bone, and part of the frontal bone. A dental drill was used to create bilateral full-thickness bone defects with a diameter of 5 mm[24] along the calvarial midline. Depending on the experimental group, scaffolds were implanted into the defects, whereas the Con group did not receive any scaffold implantation (Figure 2). The muscle and skin layers were closed using absorbable sutures.

Post-operative care consisted of intramuscular penicillin administration for infection prophylaxis; analgesic management was conducted in accordance with the approved animal protocol and ARRIVE 2.0 recommendations. Postoperatively, the animals were returned to their cages and monitored under standard housing conditions. Daily intramuscular injections of penicillin (800,000 units) were administered for three days. All rats resumed regular feeding and activity within three days, and no signs of wound infection were observed.

Animals were euthanized by overdose of sodium pentobarbital (100 mg/kg, intraperitoneally) at the designated time points (weeks 4, 8, and 12 postoperatively), followed by cervical dislocation to confirm death. Calvarial specimens were collected, fixed in 4% paraformaldehyde, and used for micro-CT analysis and histological evaluation. To assess systemic biocompatibility, blood samples were collected for hematological analysis. In addition, major organs, including the heart, liver, spleen, lungs, and kidneys, were collected for hematoxylin and eosin (H & E) staining and histopathological examination.

2.5.2. Micro-computed tomography and data analysis

At weeks 4, 8, and 12 post-implantation, calvarial specimens containing the defect site were collected and fixed in 4% paraformaldehyde for 24 h. Micro-CT images were obtained using a micro-CT scanner (ZKKS-MCT-Sharp, China), with the specimens aligned along the longitudinal axis of the scaffold. The scanning parameters were as follows: voltage = 70 kV, power = 7 W, frame averaging = 4, angular increment = 0.72°, and exposure time = 100 ms. A full 360° rotation scan was performed for each sample. Micro-CT data were analyzed using bone analysis software

Table 2. Experimental grouping

Group	Con–Con	Con–PCL	Con–TP	Con–HP	Con–HTP	PCL–TP	PCL–HP	PCL–HTP	HP–TP	HP–HTP	TP–HTP
Left defect	Con	Con	Con	Con	Con	PCL	PCL	PCL	HP	HP	TP
Right defect	Con	PCL	TP	HP	HTP	TP	HP	HTP	TP	HTP	HTP

Abbreviations: Con: Control; HP: Hydroxyapatite/polycaprolactone; HTP: Hydroxyapatite/tricalcium phosphate/polycaprolactone; PCL: Polycaprolactone; TP: Tricalcium phosphate/polycaprolactone.

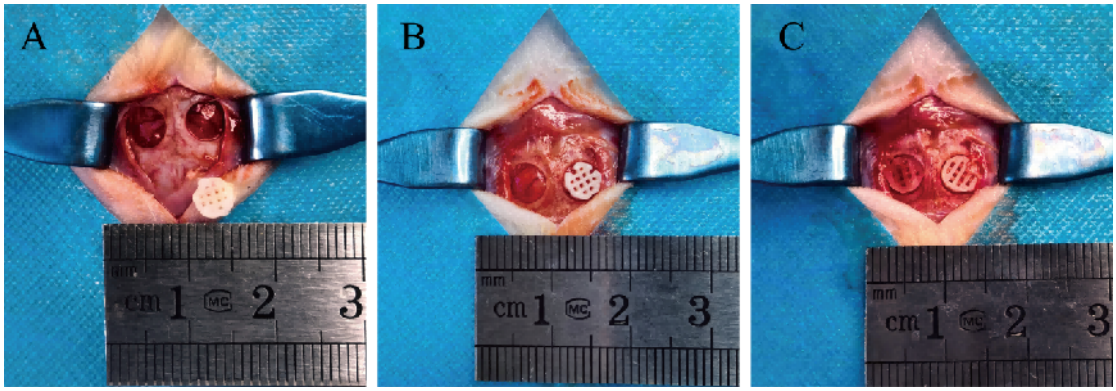

Figure 2. Establishment of the Sprague–Dawley rat calvarial defect model and scaffold implantation. (A) Macroscopic appearance of the prepared scaffolds and a schematic of the bilateral critical-sized calvarial defect model in rats (diameter = 5 mm, thickness = 1 mm). (B) Unilateral scaffold implantation into a single defect site. (C) Bilateral scaffold implantation into both defect sites.

(CTAn, Chinese version 2.0, Bruker, Kontich, Belgium) to quantify total volume (TV), BV, bone volume fraction (BV/TV), and bone mineral density (BMD).

2.5.3. Histological analysis

After the micro-CT scan, the calvarial specimens were decalcified in ethylenediaminetetraacetic acid solution (catalog no. G1105, Servicebio, Wuhan, China) at 4 °C for 35 days. Once decalcification was complete, samples from the defect center were collected, embedded in paraffin, and sectioned into 5 μm-thick slices. Tissue sections were stained with H & E (catalog no. G1003, Servicebio, Wuhan, China) and Masson's trichrome staining kits (catalog no. G1006, Servicebio, Wuhan, China) according to the manufacturer's instructions.

For immunofluorescence staining, two consecutive sections from each sample were selected to identify macrophage phenotypes. After washing with PBS, the sections were blocked with goat serum and incubated overnight at 4 °C with an anti-iNOS antibody (1:2,500) for M1-type macrophages. After incubation with the corresponding secondary antibody, a tyramide signal amplification reagent was added, followed by incubation in the dark for 10 min. Sections were then subjected to antigen retrieval using a microwave method. The sections were incubated with anti-CD163 (1:2,000) for M2-type macrophages and the corresponding secondary antibody. The cell nuclei were stained with 4',6-diamidino-2-phenylindole (Abcam, UK). The stained sections were imaged using a fluorescence microscope (NIKON Eclipse C1, Nikon, Japan).

To detect osteogenic and angiogenic markers, sections were blocked with 10% donkey serum and incubated overnight at 4 °C in a humidified chamber with a mixed solution containing anti–BMP-2 (1:200) and anti-VEGF (1:1,000) primary antibodies. Sections were incubated with the appropriate secondary antibody in the dark for 50 min, and cell nuclei were counterstained with 4',6-diamidino-2-phenylindole.

2.6. Statistical analysis

Experimental data are expressed as mean ± standard deviation. All statistical analyses were performed using GraphPad Prism software (version 10.0.0, GraphPad Software, Inc., La Jolla, CA, USA). For *in vitro* experiments, differences among groups were assessed by one-way ANOVA followed by Dunnett's multiple comparison test. For *in vivo* experiments, a linear mixed-effects model was applied. Scaffold type and time were treated as fixed effects, and the individual animal was included as a random effect to account for within-animal correlation arising from the bilateral calvarial defect design. Accordingly, measurements from the left and right defects within the same animal were treated as correlated rather than independent observations. The animal, rather than the defect, was considered the statistical unit. A p-value < 0.05 was considered statistically significant.

3. Results

3.1. Characterization of three-dimensional–printed scaffolds

Four types of scaffolds, PCL, HP (HA/PCL; 1:4), TP (TCP/PCL; 1:4), and HTP (HA/TCP/PCL; 1:1:4), were successfully fabricated using 3D printing technology. As shown in Figure 3A, macroscopic observation revealed that all scaffolds exhibited regular porous architectures with well-organized fibers and uniform layer stacking. SEM images further revealed the microscopic morphology of the scaffolds: the surface of the pure PCL scaffold was relatively smooth, whereas the HP, TP, and HTP scaffolds

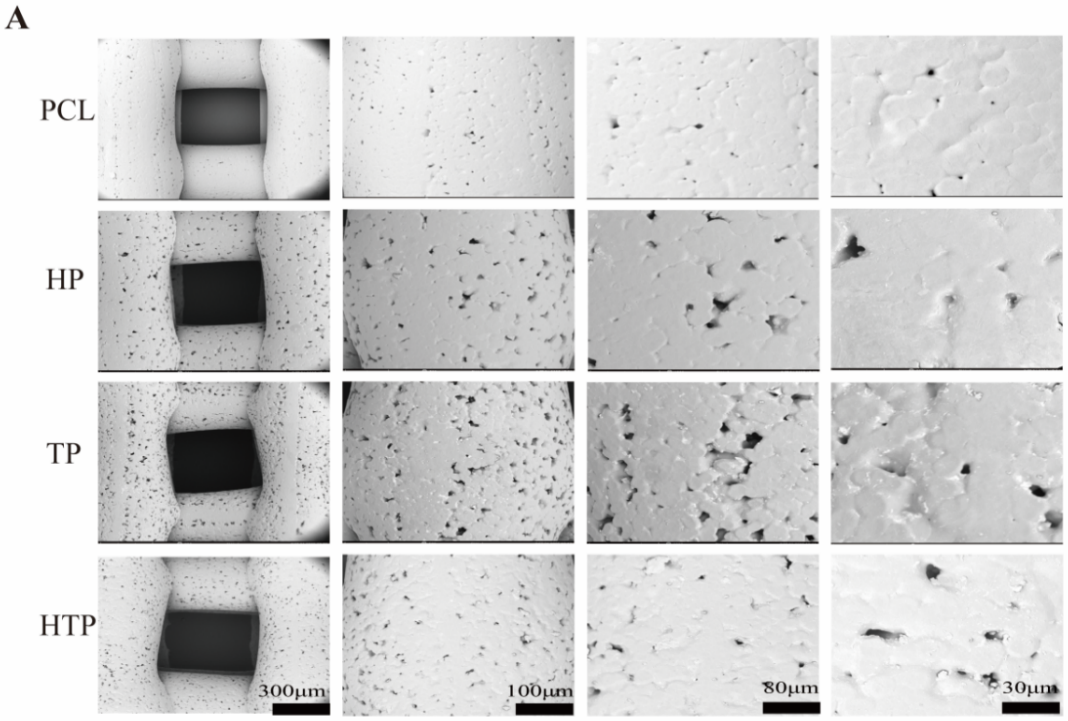

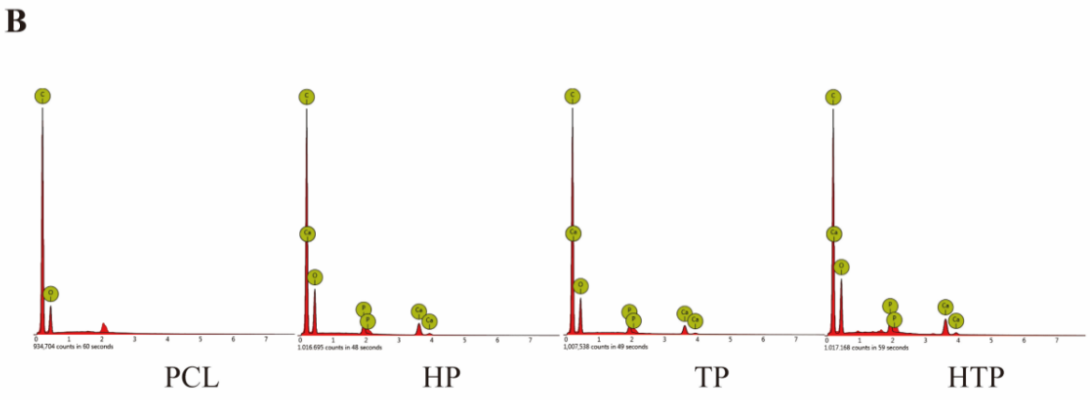

C

Sample name	C (%)	O (%)	Ca (%)	P (%)
PCL	73.76	26.24	0	0
HP	65.08	29.68	3.43	1.82
TP	68.62	27.11	2.8	1.47
HTP	61.52	32.24	4.28	1.97

Figure 3. Surface morphology and elemental composition of 3D-printed PCL, HP, TP, and HTP scaffolds. (A) Scanning electron microscope images of the four scaffolds (scale bar = 300 μm, magnification = 8×; scale bar = 100 μm, magnification = 25×; scale bar = 80 μm, magnification = 32×; scale bar = 30 μm, magnification = 64×). (B, C) Energy-dispersive X-ray spectroscopy analysis of the scaffold surface elements.
Abbreviations: C: Carbon; Ca: Calcium; HP: Hydroxyapatite/polycaprolactone; HTP: Hydroxyapatite/tricalcium phosphate/polycaprolactone; O: Oxygen; P: Phosphorus; PCL: Polycaprolactone; TP: Tricalcium phosphate/polycaprolactone.

displayed a distinctly rough and granular surface, attributed to the distribution of HA and TCP ceramic particles within the PCL matrix. At higher magnification (scale bar = 30 μm; magnification = 64×, the uniform distribution of ceramic particles on the surface of the scaffold fibers was clearly observed.

Surface elemental analysis using energy-dispersive X-ray spectroscopy (Figure 3B and 3C) showed that, compared to the pure PCL scaffold, the HP, TP, and HTP scaffolds containing ceramic components exhibited the presence of calcium and phosphorus elements. Among them, the HTP scaffold had a higher calcium-to-phosphorus ratio than the HP and TP groups, confirming the successful incorporation of HA and TCP into the composite scaffold and indicating an increased proportion of mineral components relevant to bone regeneration.

Thermogravimetric analysis (Figure 4A) showed the thermal decomposition curves of the scaffolds from room temperature to 800 °C. The pure PCL scaffold underwent complete thermal decomposition at around 400 °C, with a residual mass approaching zero. In contrast, the HP, TP, and HTP scaffolds exhibited significant residual mass at high temperatures, corresponding to the inorganic ceramic content. The residual mass of the HTP scaffold was between that of HP and TP, confirming the successful incorporation of HA and TCP into the composite scaffold.

Water contact angle measurements were used to assess the surface hydrophilicity of the scaffolds (Figure 4B and 4C). The results showed that the pure PCL scaffold exhibited the largest water contact angle, demonstrating pronounced hydrophobicity. In comparison, the water contact angles of the HP, TP, and HTP scaffolds were significantly reduced, with the HTP scaffold showing the smallest water contact angle and the highest hydrophilicity ($p < 0.001$). This indicates that the introduction of HA and TCP effectively improves the surface wettability of the PCL scaffold, which may support cell adhesion and spreading.

The porosity results (Figure 4D) showed that the porosity of all four scaffold groups remained at similarly high levels, with no significant differences between the groups ($p > 0.05$), indicating that the incorporation of the inorganic phases did not significantly affect the overall porous structure of the scaffolds.

Mechanical performance testing results (Figure 4E) showed that, compared to the pure PCL scaffold, the HP, TP, and HTP scaffolds containing ceramic components exhibited an increased compressive modulus. Among them, the HTP scaffold had the highest compressive modulus, superior to the PCL and TP groups ($p < 0.05$), and second only to the HP group, indicating that the synergistic effect of HA and TCP can effectively enhance the mechanical strength of the scaffold.

To further characterize the degradation-related behavior of the ceramic-containing scaffolds, the release profiles of Ca^{2+} and PO_4^{3-} were evaluated in the HP, TP, and HTP groups. As shown in Figure 5, all three ceramic-containing scaffolds released detectable amounts of Ca^{2+} and PO_4^{3-} during immersion, although the release patterns varied among groups. On day 1, the HP group exhibited the highest concentrations of both Ca^{2+} and PO_4^{3-}, whereas the TP and HTP groups exhibited lower but comparable levels. By day 3, the daily ion release in the HP group had decreased markedly, while the TP and HTP groups maintained relatively stable release levels. Notably, the HTP group displayed a more gradual release pattern over time, without a pronounced initial burst (Figure 5A and 5B).

The cumulative release profiles further showed that the concentrations of both Ca^{2+} and PO_4^{3-} increased with soaking time in all groups. Among them, the HP group exhibited the highest cumulative ion release, followed by the TP group, whereas the HTP group showed slightly lower cumulative values. Nevertheless, compared with the HP group, the HTP scaffold displayed a relatively stable and moderate ion release pattern throughout the observation period (Figure 5C and 5D). These findings indicate that the combined incorporation of HA and TCP altered the ion release kinetics of the scaffold and generated a relatively stable Ca/P ionic microenvironment.

3.2. *In vitro* cellular compatibility of scaffolds

To evaluate the biocompatibility of each group of scaffolds, BMSCs were seeded onto the scaffold surfaces, and cell proliferation was assessed using the CCK-8 assay. As shown in Figure 6A, on day 1 of culture, there were no significant differences in the number of cells among the groups. As the culture progressed, all groups showed increased cell proliferation. By days 3 and 7, the cell proliferation rates in the HP, TP, and HTP groups were significantly higher than those in the pure PCL group ($p < 0.05$), with the HTP group demonstrating the highest cell proliferation capacity ($p < 0.01$).

The live/dead cell staining (Figure 6B) further confirmed these findings. After three days of culture, live cells (green fluorescence) were observed on the surfaces of the scaffolds in all groups. Compared to the PCL group, the HP, TP, and HTP scaffolds showed a higher density of live cells on their surfaces, with more extensive cell spreading and well-preserved cell morphology. These results indicate that all scaffolds possess good cellular compatibility, and composite scaffolds containing ceramic components,

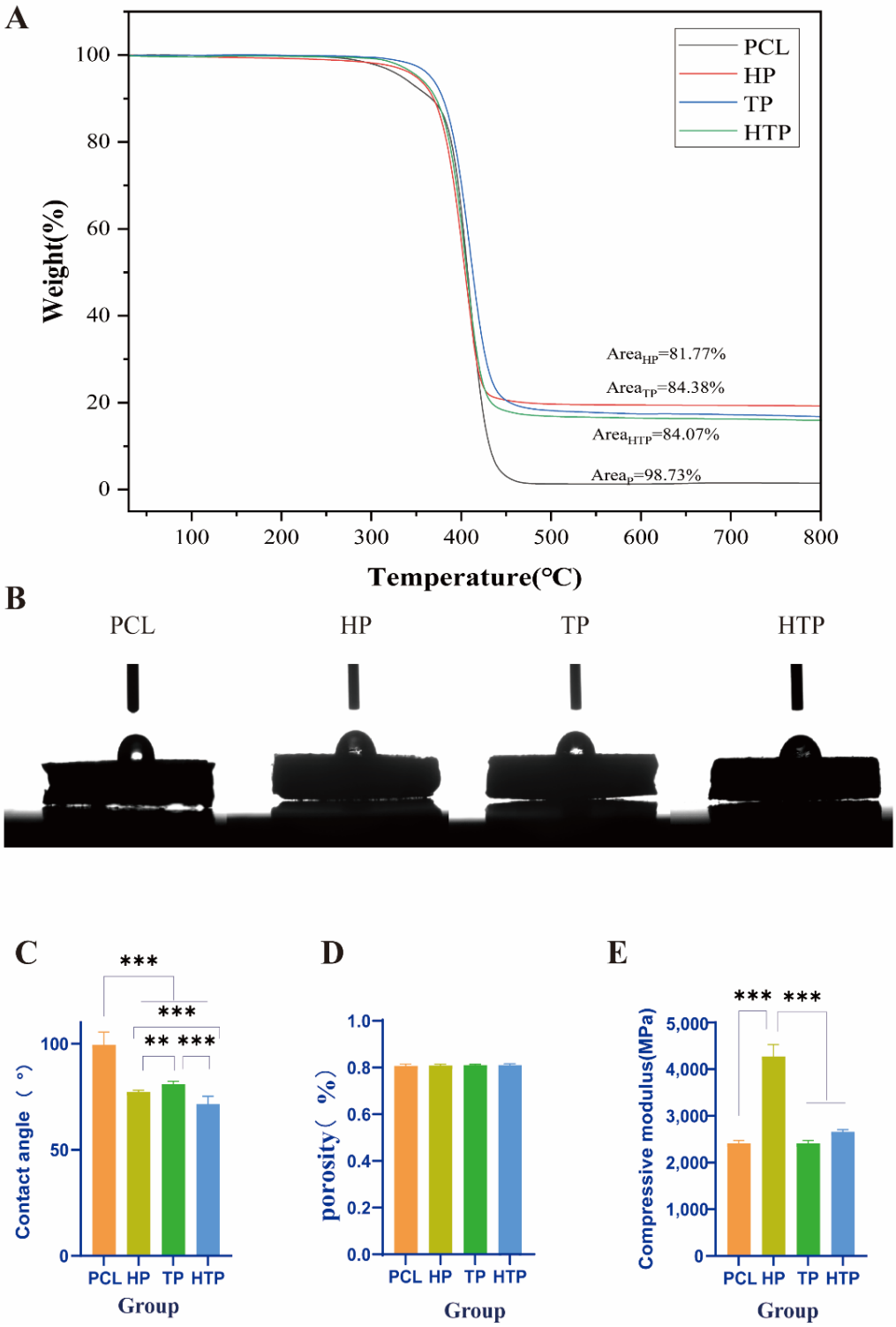

Figure 4. Physicochemical and mechanical properties of 3D-printed PCL, HP, TP, and HTP scaffolds. (A) Thermogravimetric analysis curves showing the thermal decomposition of the four scaffolds from room temperature to 800°C. (B) Representative images of water contact angle measurements on the surfaces of different scaffolds. (C–E) Quantitative analysis of the (C) water contact angle, (D) porosity, and (E) compressive modulus. Data are expressed as mean ± standard deviation. $^{**}p < 0.01$ and $^{***}p < 0.001$ indicate statistical significance.

Abbreviations: HP: Hydroxyapatite/polycaprolactone; HTP: Hydroxyapatite/tricalcium phosphate/polycaprolactone; PCL: Polycaprolactone; TP: Tricalcium phosphate/polycaprolactone.

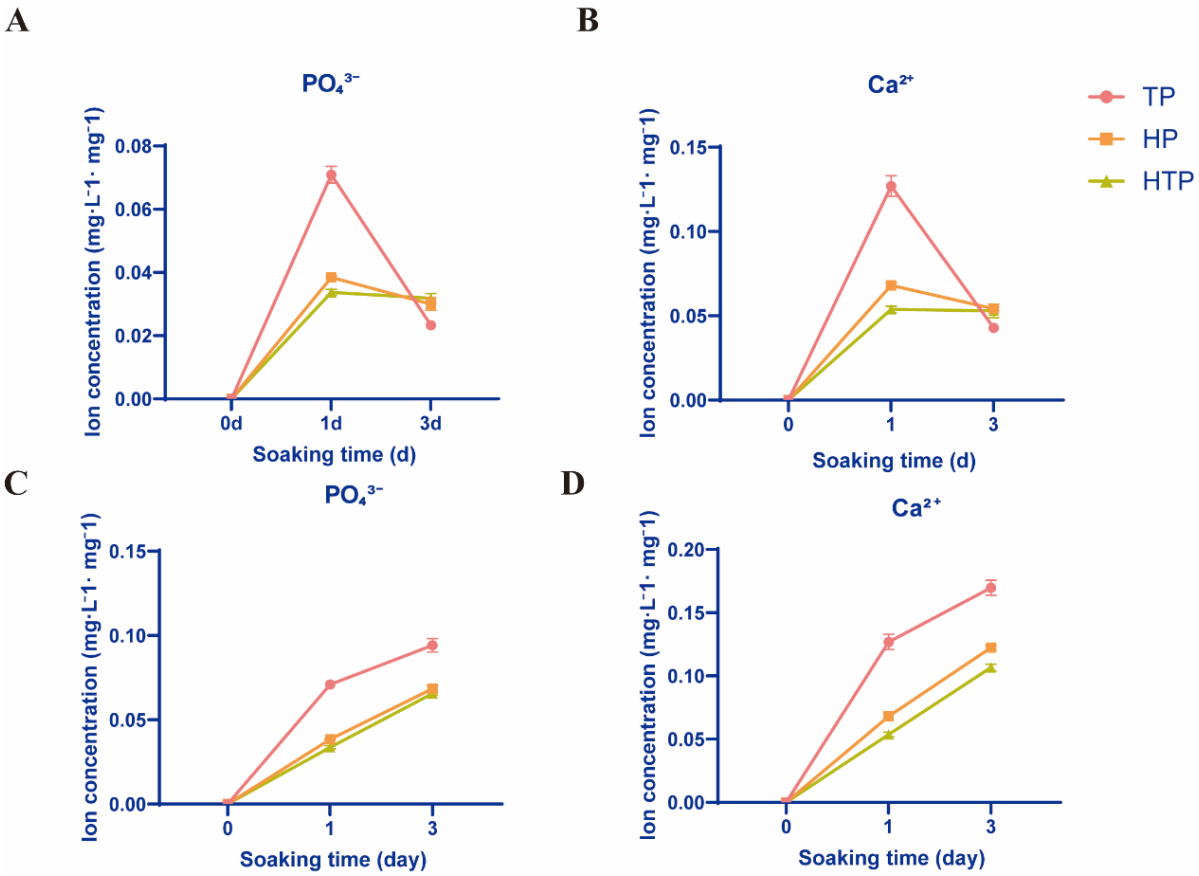

Figure 5. *In vitro* ion release behavior of ceramic-containing scaffolds. (A, B) Concentrations of (A) PO_4^{3-} and (B) Ca^{2+} released from HP, TP, and HTP scaffolds at days 1 and 3. (C, D) Cumulative release profiles of (C) PO_4^{3-} and (D) Ca^{2+} from HP, TP, and HTP scaffolds over time. Data are normalized to scaffold mass and presented as mean ± standard deviation ($n = 3$).
Abbreviations: HP: Hydroxyapatite/polycaprolactone; HTP: Hydroxyapatite/tricalcium phosphate/polycaprolactone; TP: Tricalcium phosphate/polycaprolactone.

especially the HTP scaffold, can more effectively support BMSC adhesion and proliferation.

3.3. HTP scaffold promotes BMSC osteogenic differentiation

To investigate the effects of each scaffold on BMSC osteogenic differentiation, qRT-PCR was performed to measure the expression levels of osteogenic-related genes on days 7 and 14 of osteogenic induction. As shown in Figure 7, compared to the PCL group, the HP, TP, and HTP groups exhibited higher expression of osteogenic marker genes at both time points. Specifically, *Alp* expression (Figure 7A) was significantly higher in the HTP group on days 7 and 14 compared to the other groups ($p < 0.001$). *Runx2*, a key regulator of osteogenic differentiation, exhibited the highest expression (Figure 7B) in the HTP group, significantly outperforming the PCL, HP, and TP groups ($p < 0.001$). The expression trends of *Opn* (Figure 7C) and *Col1a1* (Figure 7D) were consistent, with the HTP group exhibiting the strongest upregulation. Additionally, *Bmp2* expression (Figure 7E) was also highest in the HTP group ($p < 0.001$), indicating that the HTP scaffold promotes osteogenic differentiation by enhancing the BMP-2 signaling pathway.

To further validate the osteoinductive capacity of the scaffolds, direct osteogenic induction assays were conducted using Alizarin Red S staining and ALP staining (Figure 8). In the direct osteogenesis model, BMSCs were cultured in osteogenic medium containing scaffolds for seven days prior to staining. The results showed that ALP staining intensity and calcium deposition (Alizarin Red S staining) were more pronounced in the HTP group than in the other groups (Figure 8A and 8B). As shown in Figure 8C and 8D, semi-quantitative analysis further confirmed that ALP staining intensity and calcium deposition in the HTP group were approximately 2- and 2.5-fold higher than those in the PCL group, respectively ($p < 0.001$).

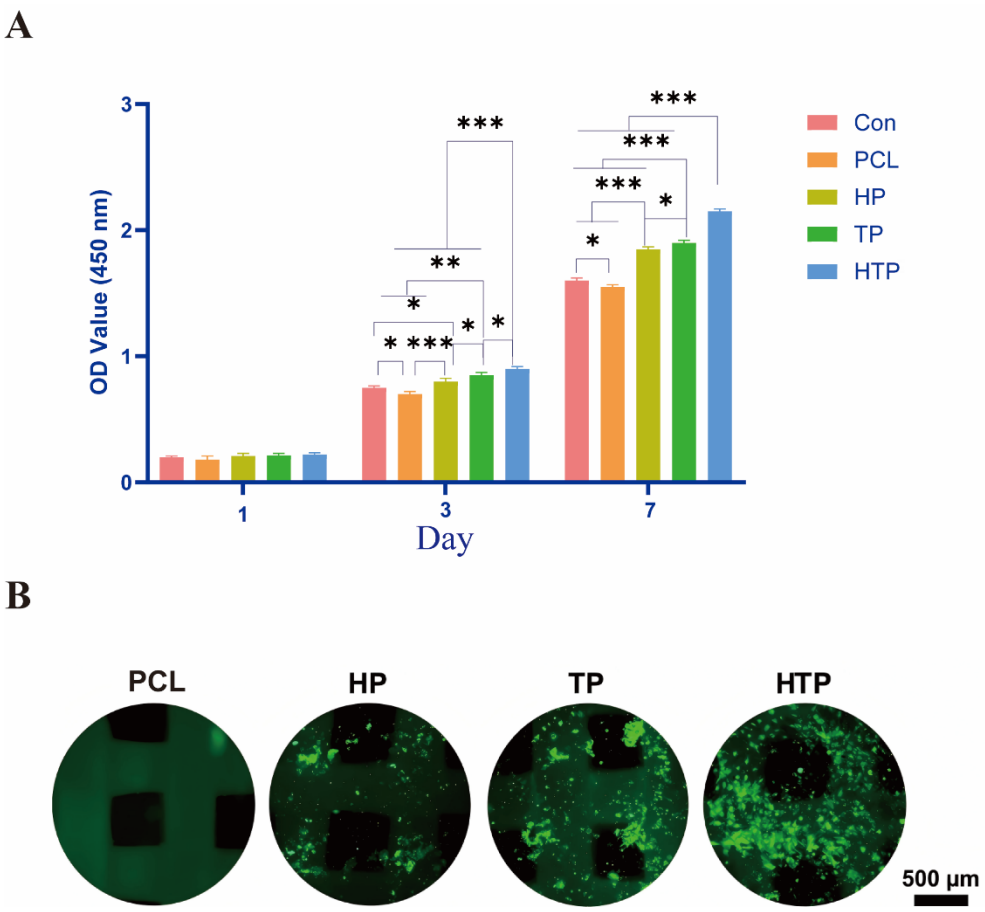

Figure 6. Biocompatibility of scaffold materials. (A) Proliferation and viability of bone marrow-derived mesenchymal stem cells on scaffolds after culture for 1, 3, and 7 days. (B) Live/dead cell staining results of the cells cultured with scaffolds for three days (scale bar = 500 μm; magnification = 10×). *$p < 0.05$, **$p < 0.01$, and ***$p < 0.001$ indicate statistical significance.
Abbreviations: Con: Control; HP: Hydroxyapatite/polycaprolactone; HTP: Hydroxyapatite/tricalcium phosphate/polycaprolactone; OD: Optical density; PCL: Polycaprolactone; TP: Tricalcium phosphate/polycaprolactone.

3.4. HTP scaffold regulates macrophage polarization toward the M2 phenotype

Macrophages play a key role in regulating the bone immune microenvironment. To explore the effects of each scaffold on macrophage polarization, RAW264.7 cells were seeded onto the surface of the scaffolds, and the expression of M1 and M2 polarization markers was assessed on days 1 and 3.

As shown in Figure 9A and 9B, the expression levels of M1 macrophage marker genes *Il1b* and *Tnfa* on day 1 and day 3 of culture were significantly lower in the HTP group compared to the PCL group ($p < 0.001$). This indicates that the HTP scaffold suppresses macrophage polarization toward the pro-inflammatory M1 phenotype.

Meanwhile, the expression levels of the M2 macrophage marker genes *Mrc1* and *Arg1* (Figure 9C and 9D) were significantly higher in the HTP group than in the other groups ($p < 0.001$) on day 1 of culture. This indicates that the HTP scaffold promotes macrophage polarization toward the anti-inflammatory/repair-oriented M2 phenotype.

Additionally, ELISA results (Figure 9E and 9F) showed that the concentration of the pro-inflammatory cytokine IL-12 in the HTP group conditioned medium was significantly decreased, while the concentration of the anti-inflammatory cytokine IL-10 was significantly increased ($p < 0.001$), further supporting the immunomodulatory effect of the HTP scaffold. Compared with the PCL group, the HTP group showed significantly lower IL-12 concentrations and significantly higher IL-10 concentrations in conditioned medium at both days 1 and 3 ($p < 0.001$), further supporting the immunomodulatory effect of the HTP scaffold. Taken together, these results suggest that the HTP scaffold effectively regulates macrophage phenotype transition by inhibiting M1 polarization and promoting M2

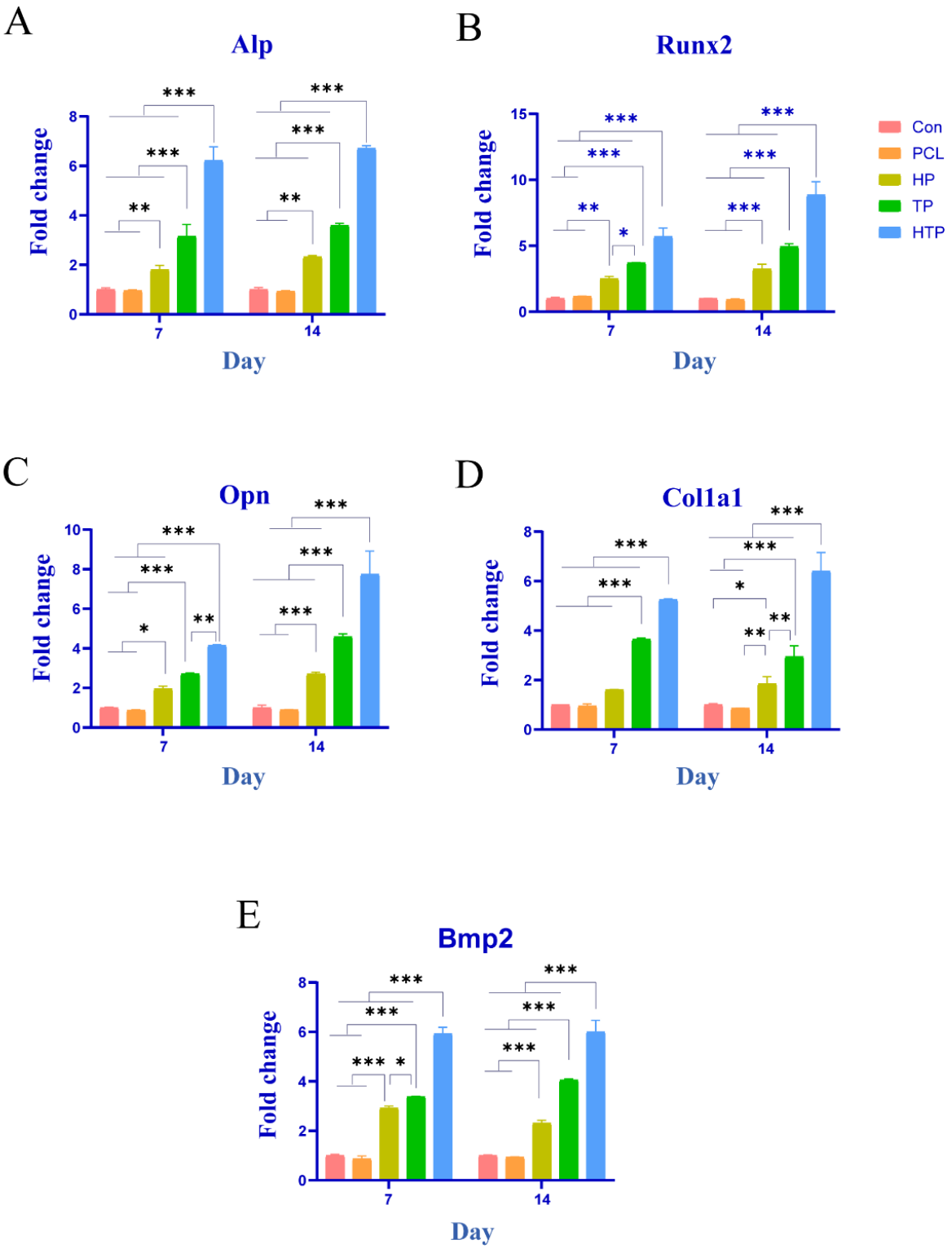

Figure 7. Expression levels of osteogenic marker genes at days 7 and 14 measured by quantitative reverse transcription polymerase chain reaction. Data are expressed as mean ± standard deviation ($n = 3$). *$p < 0.05$, **$p < 0.01$, and ***$p < 0.001$ indicate statistical significance.
Abbreviations: Con: Control; HP: Hydroxyapatite/polycaprolactone; HTP: Hydroxyapatite/tricalcium phosphate/polycaprolactone; PCL: Polycaprolactone; TP: Tricalcium phosphate/polycaprolactone.

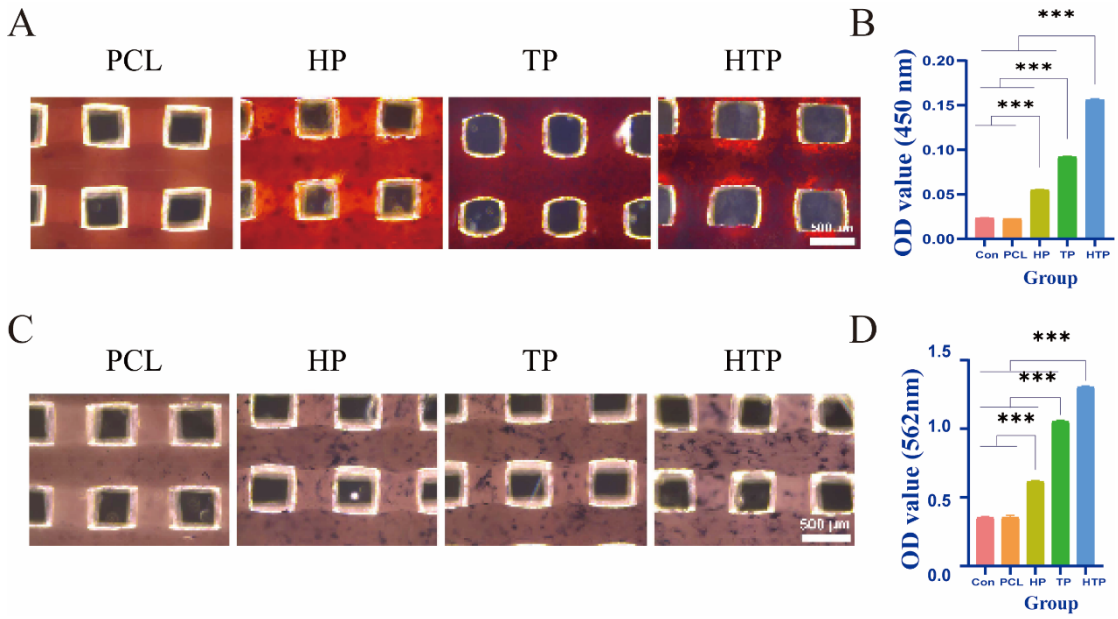

Figure 8. Osteogenic characteristics on scaffolds. (A) ALP staining results for direct osteogenesis after seven days of culture with the scaffolds (scale bar = 500 μm; magnification = 5×). (B) ALP staining intensity analysis for direct osteogenesis.(C) Alizarin Red S staining of calcium deposition after 14 days of culture with the scaffolds (scale bar = 500 μm; magnification = 5×). (D) Semi-quantitative analysis of calcium deposition by Alizarin Red S staining. ***$p < 0.001$ indicates statistical significance.

Abbreviations: ALP: Alkaline phosphatase; Con: Control; HP: Hydroxyapatite/polycaprolactone; HTP: Hydroxyapatite/tricalcium phosphate/polycaprolactone; OD: Optical density; PCL: Polycaprolactone; TP: Tricalcium phosphate/polycaprolactone.

polarization, thus creating an immune microenvironment conducive to bone regeneration.

To further verify macrophage polarization at the phenotypic level, flow cytometry was performed using CD86 and CD206 double staining (Figure 10). Representative flow cytometric plots showed that the proportion of $CD86^+CD206^-$ cells was highest in the PCL group and progressively decreased in the HP, TP, and HTP groups (Figure 10A).

Quantitative analysis confirmed that the percentage of $CD86^+CD206^-$ cells decreased from 12.7% in the PCL group to 10.1% in the HP group, 8.26% in the TP group, and 5.39% in the HTP group (Figure 10B). In contrast, the proportion of $CD86^-CD206^+$ cells increased from 6.13% in the PCL group to 15.0% in the HP group, 19.8% in the TP group, and 24.3% in the HTP group, with the HTP group showing the highest proportion among all groups (Figure 10C).

Consistent with the qRT-PCR and ELISA findings, these flow cytometry results demonstrated that ceramic-containing scaffolds reduced the proportion of M1-like macrophages and increased the proportion of M2-like macrophages, with the HTP scaffold showing the most pronounced effect. These phenotypic data further support the ability of the HTP scaffold to shift macrophages toward a pro-regenerative polarization state.

To further quantify the osteogenic response under immuno-osteogenic conditions, the expression of osteogenesis-related genes in BMSCs was analyzed by qRT-PCR after 7 and 14 days of induction with macrophage-conditioned medium. As shown in Figure 11, the expression levels of *Alp*, *Bmp2*, *Col1a1*, *Opn*, and *Runx2* were low in the Con and PCL groups but were markedly increased in the HP, TP, and HTP groups. Among all groups, the HTP group consistently showed the highest expression levels across all five osteogenic markers at both time points.

On day 7, early osteogenic markers, including *Alp* and *Runx2*, were already significantly upregulated in the HTP group compared with the other groups. By day 14, the expression levels of *Bmp2*, *Col1a1*, and *Opn* were further elevated, and the HTP group remained the highest among all groups. Overall, the expression levels of these osteogenesis-related genes were higher on day 14 than on day 7, indicating a time-dependent increase in osteogenic differentiation under immuno-osteogenic conditions. These results were consistent with the staining data and further demonstrated that macrophage-conditioned medium derived from the HTP scaffold group exerted the strongest pro-osteogenic effect on BMSCs.

To further validate the immuno-osteoinductive

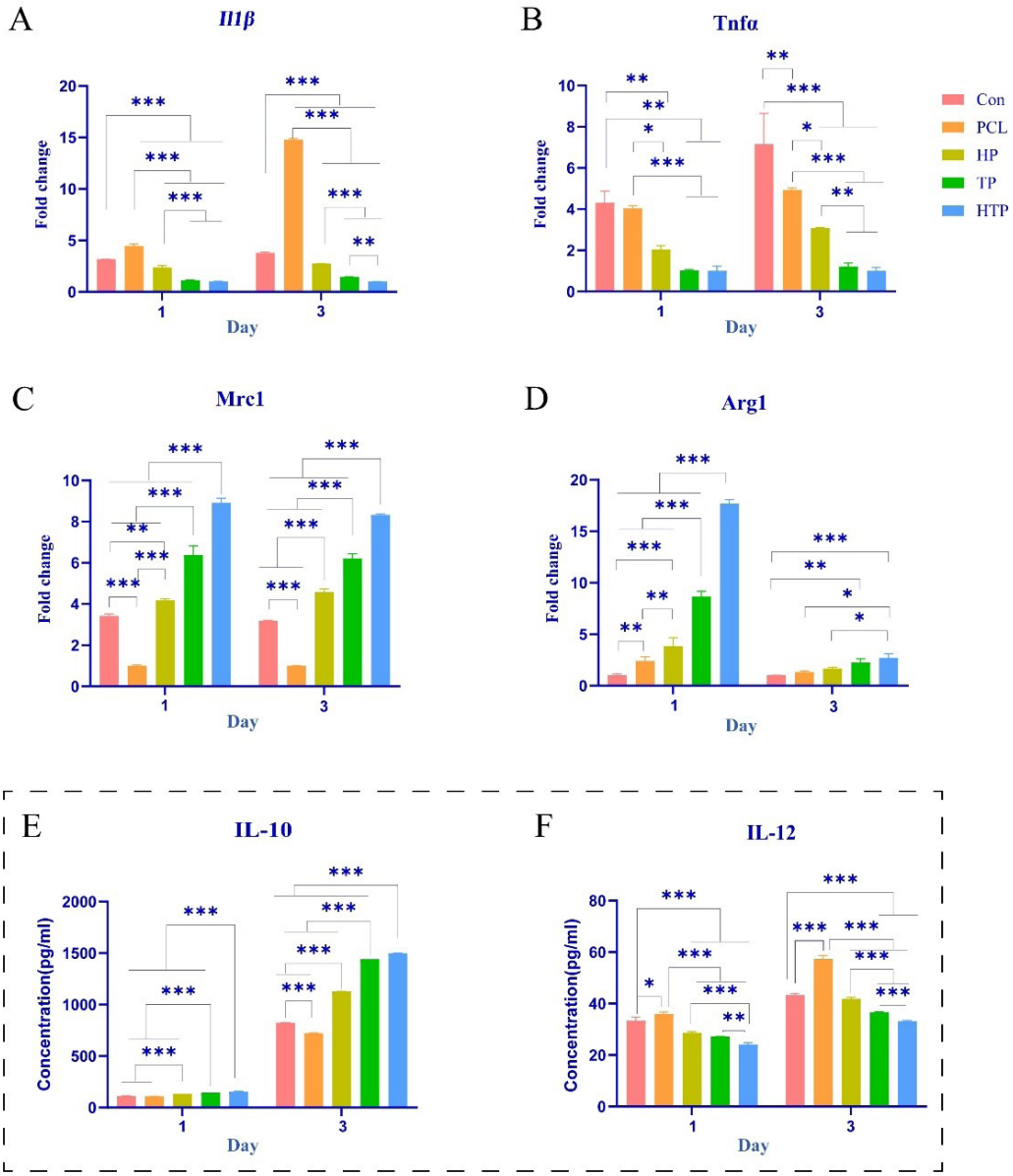

Figure 9. Polarization characteristics of macrophages on scaffolds. (A, B) Gene expression levels of M1 polarization markers in RAW264.7 cells cultured with the scaffolds. (C, D) Gene expression levels of M2 polarization markers in RAW264.7 cells cultured with the scaffolds. (E, F) Cytokine concentrations in RAW264.7 cells cultured with scaffolds. $^{*}p < 0.05$, $^{**}p < 0.01$, and $^{***}p < 0.001$ indicate statistical significance. Abbreviations: Con: Control; HP: Hydroxyapatite/polycaprolactone; HTP: Hydroxyapatite/tricalcium phosphate/polycaprolactone; IL: Interleukin; PCL: Polycaprolactone; TP: Tricalcium phosphate/polycaprolactone.

capacity of the scaffolds, immuno-osteogenesis assays were conducted using ALP and Alizarin Red S staining (Figure 12). In the immune-osteogenic model, scaffolds were first cultured with macrophages. After collecting the conditioned medium, it was mixed with osteogenic medium and used for BMSC osteogenic induction. The results showed that, under immuno-osteogenic conditions, the osteoinductive effects of all scaffolds were enhanced, with the HTP group exhibiting the highest calcium deposition and ALP staining intensity (Figure 12A and 12B). Semi-quantitative analysis further revealed that calcium deposition and ALP staining intensity in the HTP group were significantly higher than those in the other groups ($p < 0.001$) (Figure 12C and 12D). These findings indicate that the HTP scaffold not only directly promotes BMSC osteogenic differentiation but also indirectly enhances osteogenesis by modulating macrophage-derived cytokines.

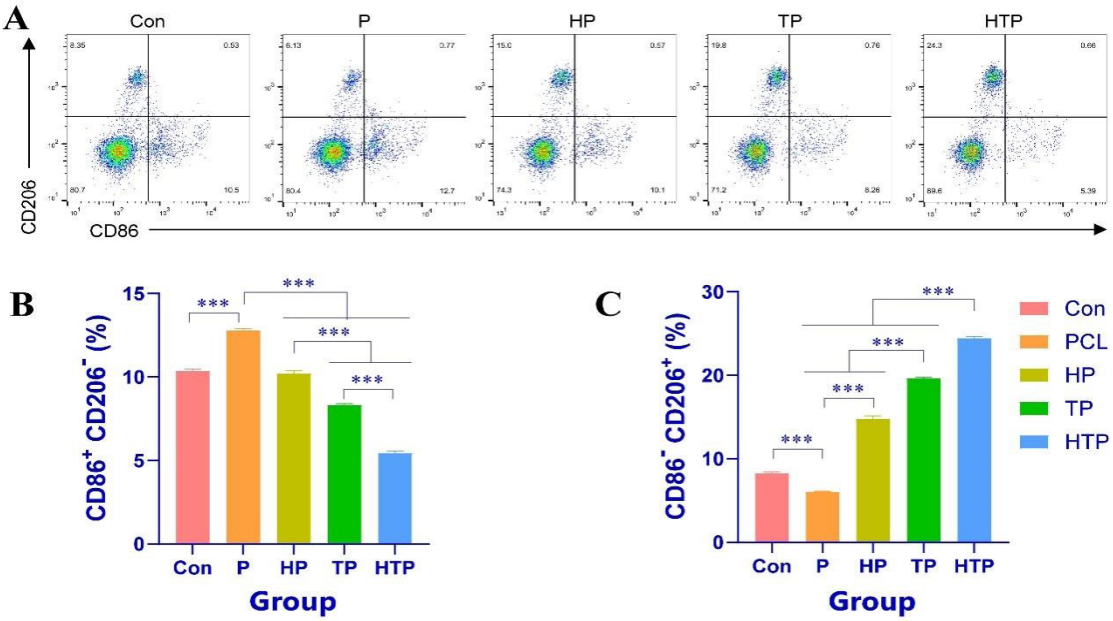

Figure 10. Flow cytometric analysis of macrophage polarization induced by different scaffolds. (A) Representative flow cytometry dot plots showing CD86 and CD206 expression in RAW264.7 macrophages cultured with different scaffolds. $CD86^+CD206^-$ cells represent M1-like macrophages, while $CD86^-CD206^+$ cells represent M2-like macrophages. (B, C) Quantitative analysis of the percentage of (B) $CD86^+CD206^-$ (M1-like) and **(C)** $CD86^-CD206^+$ (M2-like) macrophages in each group. Data are presented as mean ± standard deviation ($n = 3$). ***$p < 0.001$ indicates statistical significance.
Abbreviations: Con: Control; HP: Hydroxyapatite/polycaprolactone; HTP: Hydroxyapatite/tricalcium phosphate/polycaprolactone; PCL: Polycaprolactone; TP: Tricalcium phosphate/polycaprolactone.

3.5. *In vivo* verification of scaffold biocompatibility and osteogenic differentiation capacity

3.5.1. Micro-computed tomography imaging assessment

To assess bone defect healing, micro-CT imaging was performed in a rat calvarial defect model at weeks 4, 8, and 12 post-operation. As shown in Figure 13, the Con group, which did not receive scaffolds, exhibited minimal new bone formation at early time points (weeks 4 and 8), and no significant bone growth was observed by week 12. This indicates that intrinsic bone healing is severely limited without scaffold support.

In contrast, the PCL group, which received pure PCL scaffolds, showed limited bone regeneration. A small amount of bone formed by week 4, and although new BV increased at weeks 8 and 12, large defect areas remained, highlighting the restricted repair capacity of pure PCL scaffolds. The HP and TP groups showed enhanced new bone formation compared to the PCL group at all time points. Notably, the HTP group exhibited significantly greater bone formation at weeks 4 and 8. By week 12, the HTP group displayed well-developed trabecular and lamellar bone structures along the scaffold, with the defect area nearly completely filled with newly formed bone.

Additionally, micro-CT quantitative analysis showed that both BV/TV and BMD increased over time in all scaffold groups, and the patterns observed in the raw data distribution, raw mean summaries, and model-based estimated marginal means were generally consistent (Figure 14A–14H). For BV/TV, values increased progressively at 1, 2, and 3 months in all groups, although the magnitude of increase differed markedly among groups. The HTP group maintained the highest level at all time points and exhibited the most pronounced increase from 2 to 3 months. The TP group ranked second overall and showed a notable upward trend at the middle and late stages. The HP group also increased over time, but remained lower than the TP group overall. In contrast, the PCL and Con groups showed relatively low values, with only limited increases over time. Notably, the difference between the PCL and HP groups was small at the early time point, whereas from 2 months onward, the HP group was consistently higher than the PCL group (Figure 14A, 14B, and 14D). Visualization of the paired bilateral design further showed that, in most paired comparisons, the side implanted with the higher-performing scaffold exhibited higher BV/TV than the corresponding control or lower-performing side, and this difference became more evident at 3 months (Figure 14C).

The trend in BMD was generally consistent with that

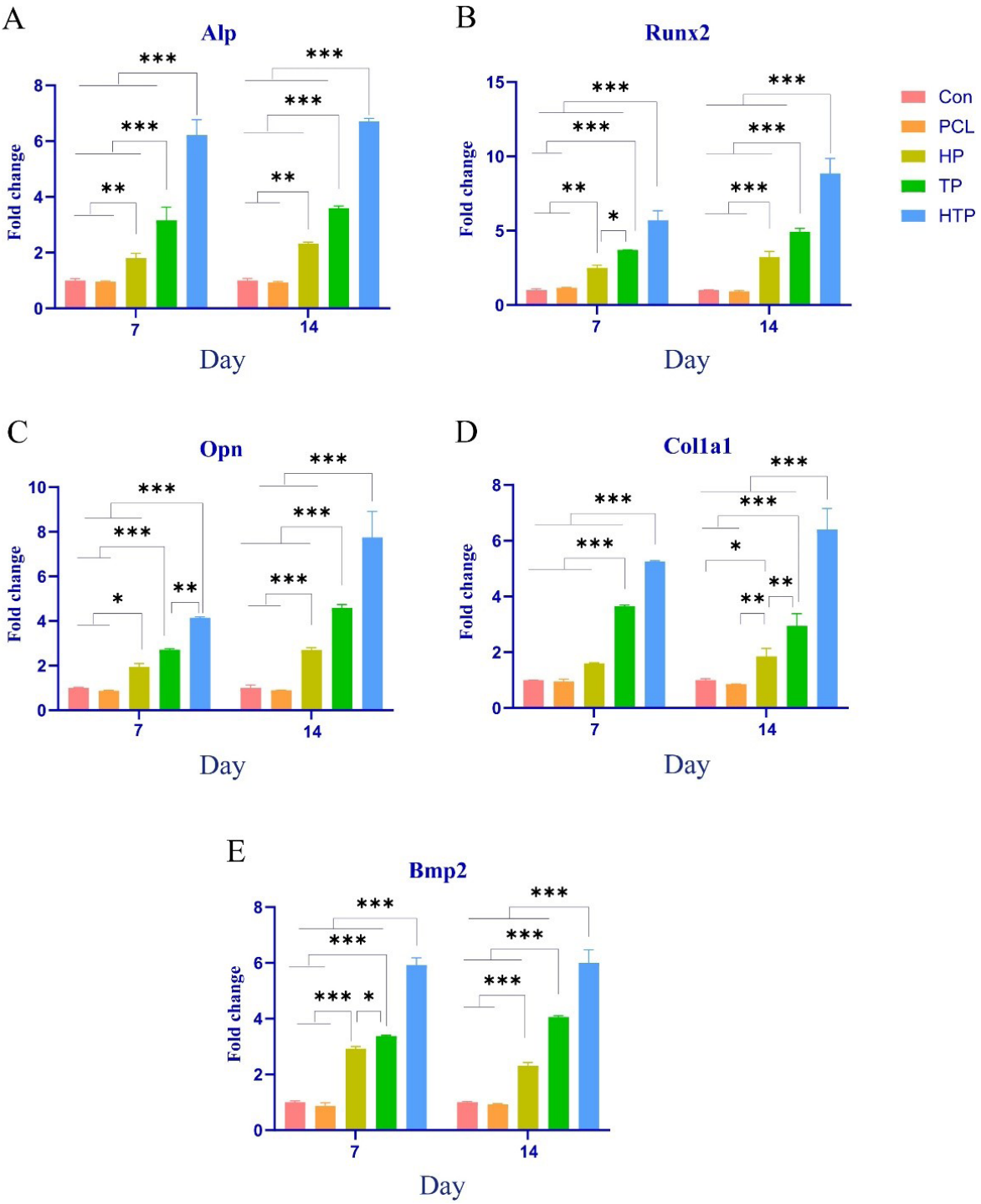

Figure 11. Expression of osteogenesis-related genes in BMSCs under immuno-osteogenic conditions, using macrophage-conditioned medium derived from different scaffold groups at days 7 and 14. ***$p < 0.001$ indicates statistical significance.
Abbreviations: Con: Control; HP: Hydroxyapatite/polycaprolactone; HTP: Hydroxyapatite/tricalcium phosphate/polycaprolactone; PCL: Polycaprolactone; TP: Tricalcium phosphate/polycaprolactone.

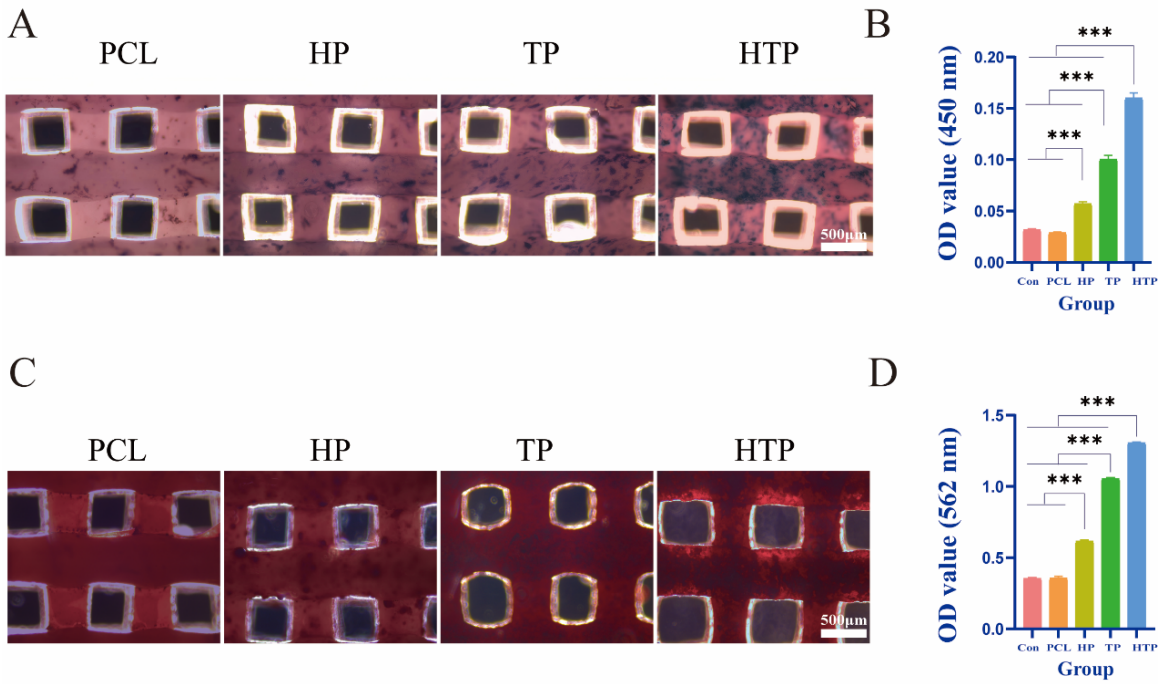

Figure 12. Immuno-osteogenic differentiation capacity of scaffolds assessed by ALP and Alizarin Red S staining. (A) Immuno-osteogenesis ALP staining results after seven days of culture with the scaffolds (scale bar = 500 μm; magnification = 5×). (C) Immuno-osteogenesis Alizarin Red S staining results after 14 days of culture with the scaffolds. (B, D) Semi-quantitative analysis of (B) ALP staining intensity and (D) Alizarin Red S staining intensity in immuno-osteogenesis. ***$p < 0.001$ indicates statistical significance.
Abbreviations: ALP: Alkaline phosphatase; Con: Control; HP: Hydroxyapatite/polycaprolactone; HTP: Hydroxyapatite/tricalcium phosphate/polycaprolactone; OD: Optical density; PCL: Polycaprolactone; TP: Tricalcium phosphate/polycaprolactone.

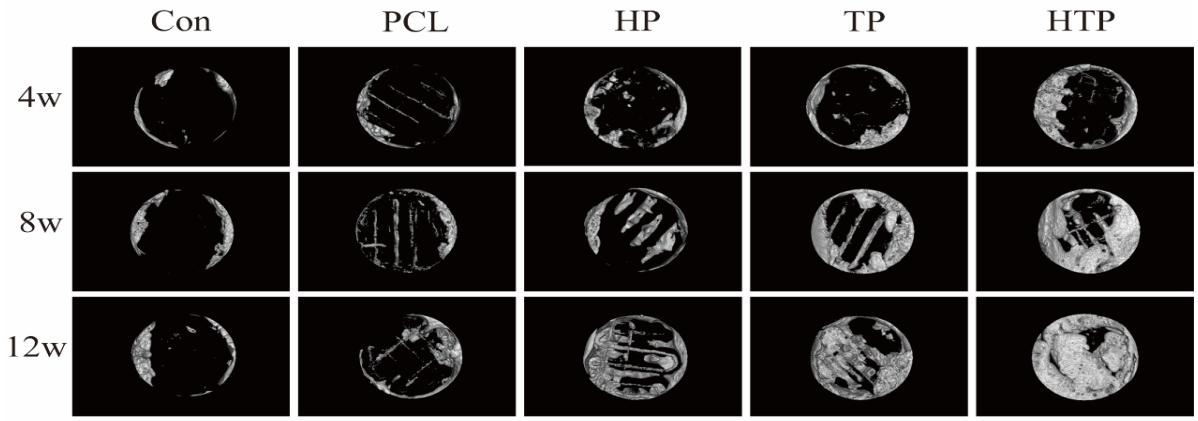

Figure 13. Micro-computed tomography analysis of scaffolds in the rat calvarial defect model showing cross-sectional images at weeks 4, 8, and 12 post-implantation.
Abbreviations: Con: Control; HP: Hydroxyapatite/polycaprolactone; HTP: Hydroxyapatite/tricalcium phosphate/polycaprolactone; PCL: Polycaprolactone; TP: Tricalcium phosphate/polycaprolactone.

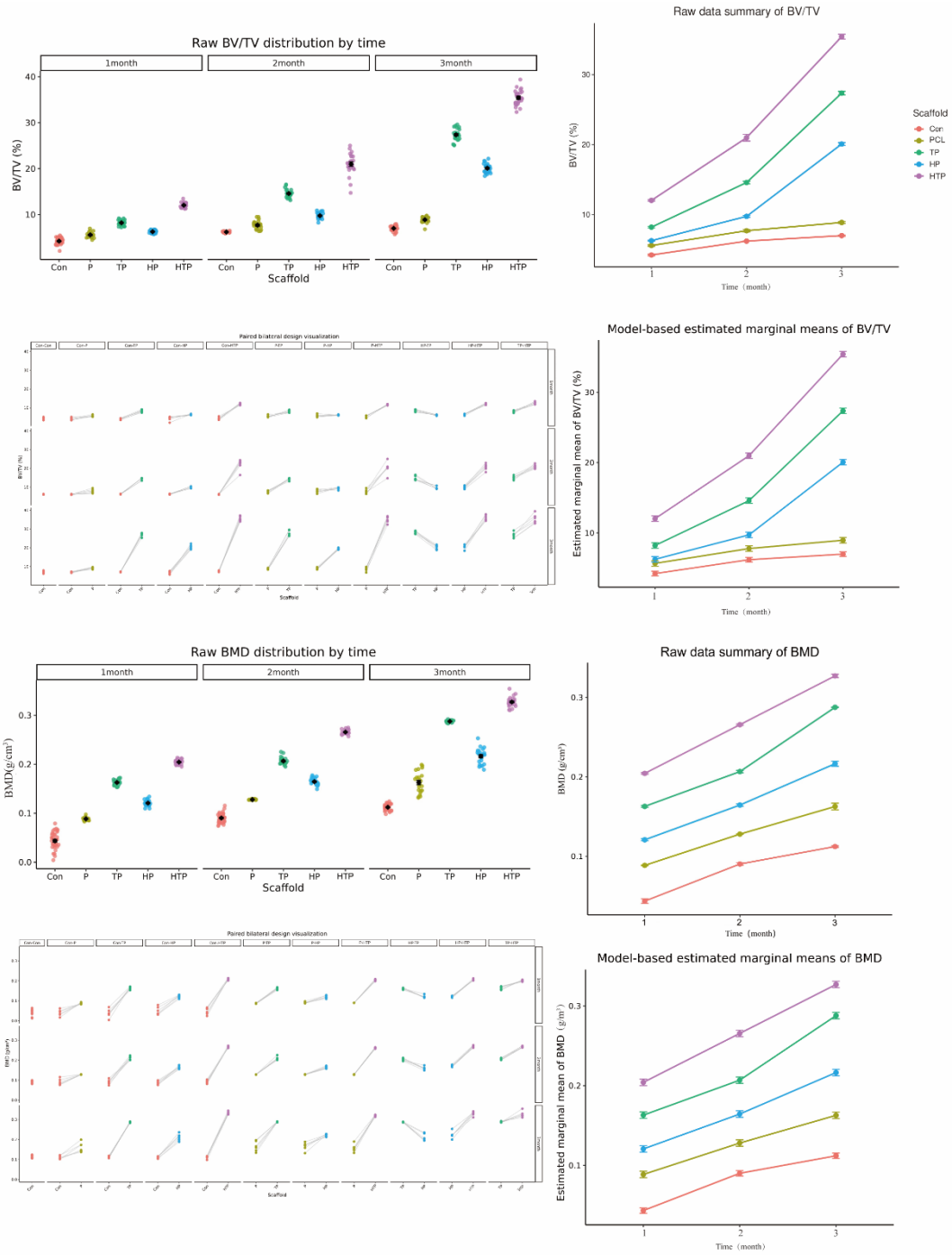

Figure 14. Dynamic changes in BV/TV and BMD during *in vivo* bone repair among different scaffold groups. (A) Raw mean trend plot of BV/TV. (B) Distribution of raw BV/TV data at each time point. (C) Paired bilateral visualization of BV/TV within individual animals. (D) Model-derived estimated marginal means of BV/TV. (E) Raw mean trend plot of BMD at each time point. (F) Distribution of raw BMD data at each time point. (G) Paired bilateral visualization of BMD within individual animals. (H) Model-derived estimated marginal means of BMD. Both BV/TV and BMD increased over time in all groups, with the HTP group consistently showing the highest values, followed by TP and HP, whereas PCL and Con remained lower. Trends observed in the raw data were consistent with the linear mixed-effects model estimates. Data are presented as mean ± standard error.

Abbreviations: BMD: Bone mineral density; BV: Bone volume; Con: Control; HP: Hydroxyapatite/polycaprolactone; HTP: Hydroxyapatite/tricalcium phosphate/polycaprolactone; PCL: Polycaprolactone; TP: Tricalcium phosphate/polycaprolactone; TV: Total volume.

of BV/TV. BMD increased progressively over time in all groups, with the HTP group showing the highest values at 1, 2, and 3 months, followed by the TP group, the HP group, and then the PCL and Con groups (Figure 14E, 14F, and 14H). Similar to BV/TV, the TP, HP, and HTP groups displayed more pronounced time-dependent increases, whereas the Con group showed the smallest increase. The paired bilateral plots showed that, in most within-animal comparisons, the side implanted with the higher-performing scaffold had higher BMD than the paired side receiving a lower-grade material or control treatment, and the between-side difference became more pronounced over time (Figure 14G).

3.5.2. Histological analysis of bone regeneration

The H & E staining results (Figure 15) further revealed the histological changes in the bone defect areas after scaffold implantation in each group. At week 4 post-operation, the defect areas in the Con and PCL groups were primarily filled with fibrous connective tissue, with only a small amount of new bone formation observed at the edges of the defect. In the HP and TP groups, more new bone tissue was observed, with a more uniform distribution of bone cells. The HTP group exhibited the most prominent new bone formation, with a more mature bone tissue structure. As time progressed, new bone formation increased in all groups by weeks 8 and 12. The HTP group consistently showed the best bone regeneration results, with newly formed bone tissue tightly integrated with the scaffold material, demonstrating excellent osseointegration.

The Masson trichrome staining results (Figure 16) were used to evaluate the deposition of collagen fibers in the newly formed bone tissue. In the early postoperative period (week 4), blue-stained collagen fibers were observed in the defect areas of all groups, with the HTP group showing the most abundant collagen deposition. As bone maturation progressed, collagen fibers gradually mineralized into mature bone tissue (red staining) by weeks 8 and 12. The HTP group consistently showed the most mature bone formation at all time points, with well-aligned collagen fibers and clear trabecular bone structures. This indicates that the HTP scaffold effectively promotes bone matrix deposition and the maturation of bone tissue.

3.5.3. Immunohistochemical fluorescence staining

To explore the regulatory effect of scaffolds on the *in vivo* immune microenvironment and their relationship with angiogenesis and bone formation, triple immunofluorescence staining was performed on the calvarial defect area at postoperative weeks 4, 8, and 12 (Figure 17).

As shown in Figure 17A, 17C, and 17E, M1 and M2 macrophages were labeled with iNOS and CD163, respectively. At week 4 post-operation (Figure 17A), the defect areas in the Con and PCL groups exhibited significant infiltration of iNOS-positive M1 macrophages, with relatively few CD163-positive M2 macrophages. In contrast, the HP, TP, and HTP groups showed a significant reduction in M1 macrophages and an increase in M2 macrophages, with the HTP group showing the highest M2/M1 ratio. By weeks 8 (Figure 17C) and 12 (Figure 17E), this trend became more pronounced, with M1 macrophages in the HTP group remaining at low levels, while M2 macrophages remained highly expressed. These results suggest that the HTP scaffold continuously regulates macrophage polarization *in vivo*, promoting the transition from the pro-inflammatory M1 phenotype to the anti-inflammatory/repair-oriented M2 phenotype, thereby creating an immune microenvironment favorable for bone regeneration.

As shown in Figure 17B, 17D, and 17F, VEGF and BMP-2 were used to label angiogenesis- and bone formation-related proteins, respectively. At week 4 post-operation (Figure 17B), strong VEGF and BMP-2 signals were observed in the defect area of the HTP group, indicating the early initiation of angiogenesis and bone formation. In contrast, VEGF and BMP-2 expressions were weaker in the Con and PCL groups. By weeks 8 (Figure 17D) and 12 (Figure 17F), changes in VEGF and BMP-2 expression were observed in all groups. The HTP group consistently maintained high levels of VEGF and BMP-2 expression throughout the observation period, and both showed good co-localization, indicating a close coupling between angiogenesis and bone formation.

In summary, the HTP scaffold establishes an immune–vascular–osteogenic microenvironment favorable for bone regeneration by regulating the M1/M2 macrophage polarization balance, promoting VEGF-mediated angiogenesis, and upregulating BMP-2 expression, thereby enhancing bone repair in calvarial defects.

3.5.4. Biocompatibility of the scaffold

To assess the systemic biocompatibility of each scaffold group, blood samples from rats were collected at postoperative weeks 4, 8, and 12 for hematological testing. As shown in Table 3, the white blood cell count, red blood cell count, hemoglobin, and platelet count remained within the normal range for all groups at all time points, with no significant differences between groups ($p > 0.05$). Liver function markers (alanine aminotransferase and aspartate aminotransferase) and kidney function markers (urea and creatinine) also exhibited no abnormalities, indicating that scaffold implantation did not negatively impact liver or

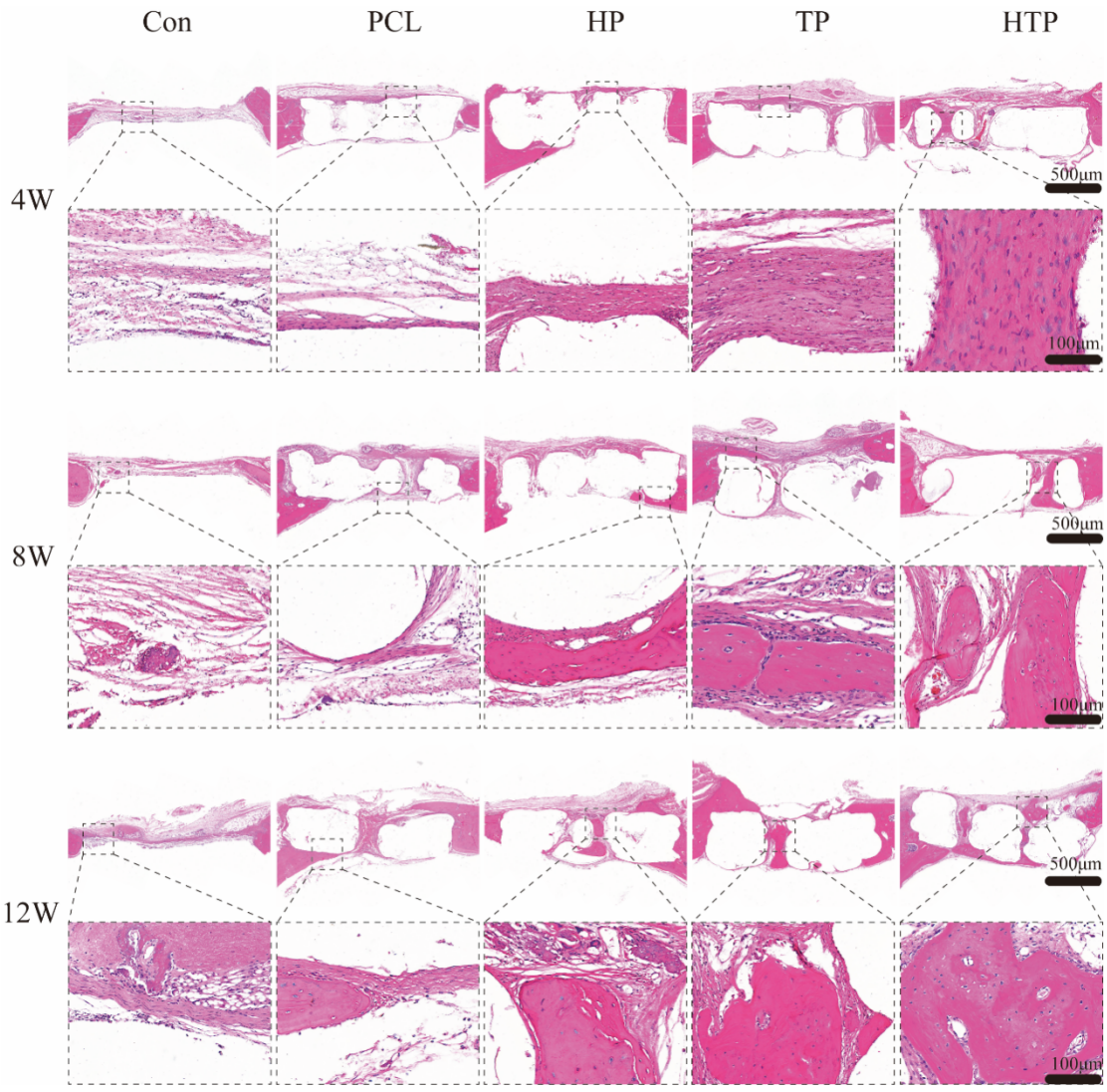

Figure 15. Hematoxylin and eosin staining of rat calvarial specimens at weeks 4, 8, and 12 post-operation (scale bar = 500 μm, magnification = 5×; scale bar = 100 μm, magnification = 25×).
Abbreviations: Con: Control; HP: Hydroxyapatite/polycaprolactone; HTP: Hydroxyapatite/tricalcium phosphate/polycaprolactone; PCL: Polycaprolactone; TP: Tricalcium phosphate/polycaprolactone.

kidney function in rats.

The histopathological examination of major organs further confirmed the biocompatibility of the scaffolds. As shown in Figures 18–20, H & E staining of the heart, liver, spleen, lung, and kidney tissues of rats at weeks 4 (Figure 18), 8 (Figure 19), and 12 (Figure 20) post-operation revealed intact tissue structures, normal cell morphology, and no significant infiltration of inflammatory cells, tissue necrosis, or fibrosis. These results indicate that the PCL, HP, TP, and HTP scaffolds all exhibit good *in vivo* biocompatibility and are suitable for bone tissue engineering applications.

4. Discussion

Insufficient immune regulation remains a major bottleneck in bone tissue engineering. Most currently available 3D-printed polymer–ceramic scaffolds are primarily designed to provide passive structural support and do not adequately address the macrophage-dominated immune microenvironment that governs early bone repair.[25] According to the osteoimmunomodulation paradigm, a timely transition of macrophages from the M1 to the M2 phenotype is essential for effective osteogenesis.[26] However, it remains poorly understood how scaffold composition alone can autonomously promote this transition in the

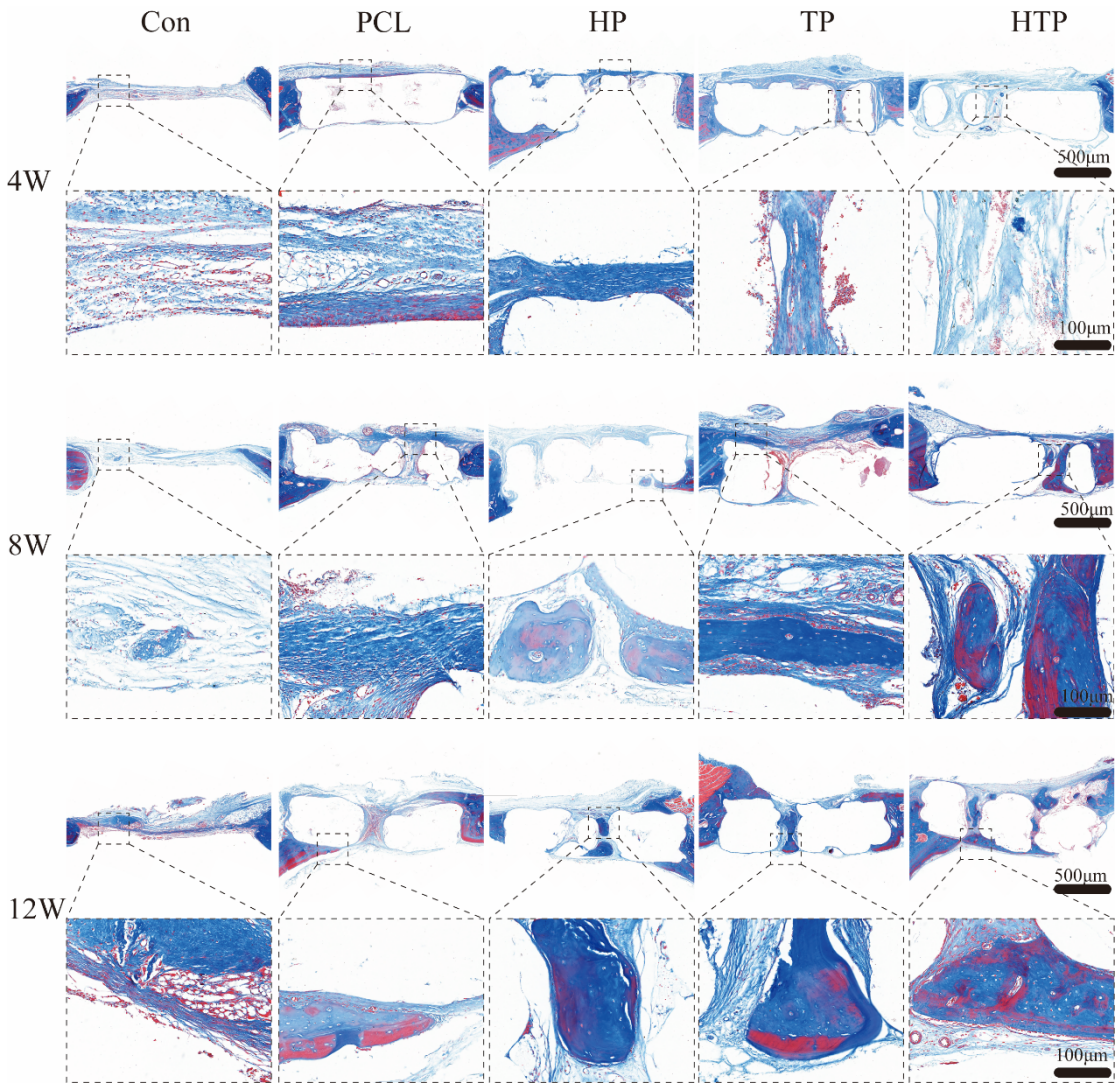

Figure 16. Masson trichrome staining of rat calvarial specimens at weeks 4, 8, and 12 post-operation (scale bar = 500 μm, magnification = 5×; scale bar = 100 μm, magnification = 25×).
Abbreviations: Con: Control; HP: Hydroxyapatite/polycaprolactone; HTP: Hydroxyapatite/tricalcium phosphate/polycaprolactone; PCL: Polycaprolactone; TP: Tricalcium phosphate/polycaprolactone.

absence of exogenous biologics.

The present study addresses this issue by developing a 3D-printed HTP composite scaffold and systematically evaluating its performance through physicochemical characterization, *in vitro* osteogenic assays, and an *in vivo* evaluation using a rat calvarial defect model. The central finding is that the co-incorporation of biphasic calcium phosphate confers synergistic physicochemical, immunomodulatory, and osteoinductive advantages that are not reproduced by single-component or binary systems, thereby providing both a mechanistic basis and a clinically relevant platform for immunomodulation-driven bone regeneration.

The HTP scaffold exhibited greater surface roughness, improved hydrophilicity, and a higher compressive modulus than all single-component and binary control scaffolds (Figures 3 and 4). These advantages may be attributed to two main factors. First, the polar hydroxyl and phosphate groups in HA help reduce the intrinsic hydrophobicity of PCL.[27] Second, the distribution of the ceramic phase between two components with distinct morphologies generates a more complex multiscale surface topography than either component alone.

Previous studies have shown that HP composites may exhibit agglomeration-related deterioration in surface uniformity when the HA content exceeds approximately 40

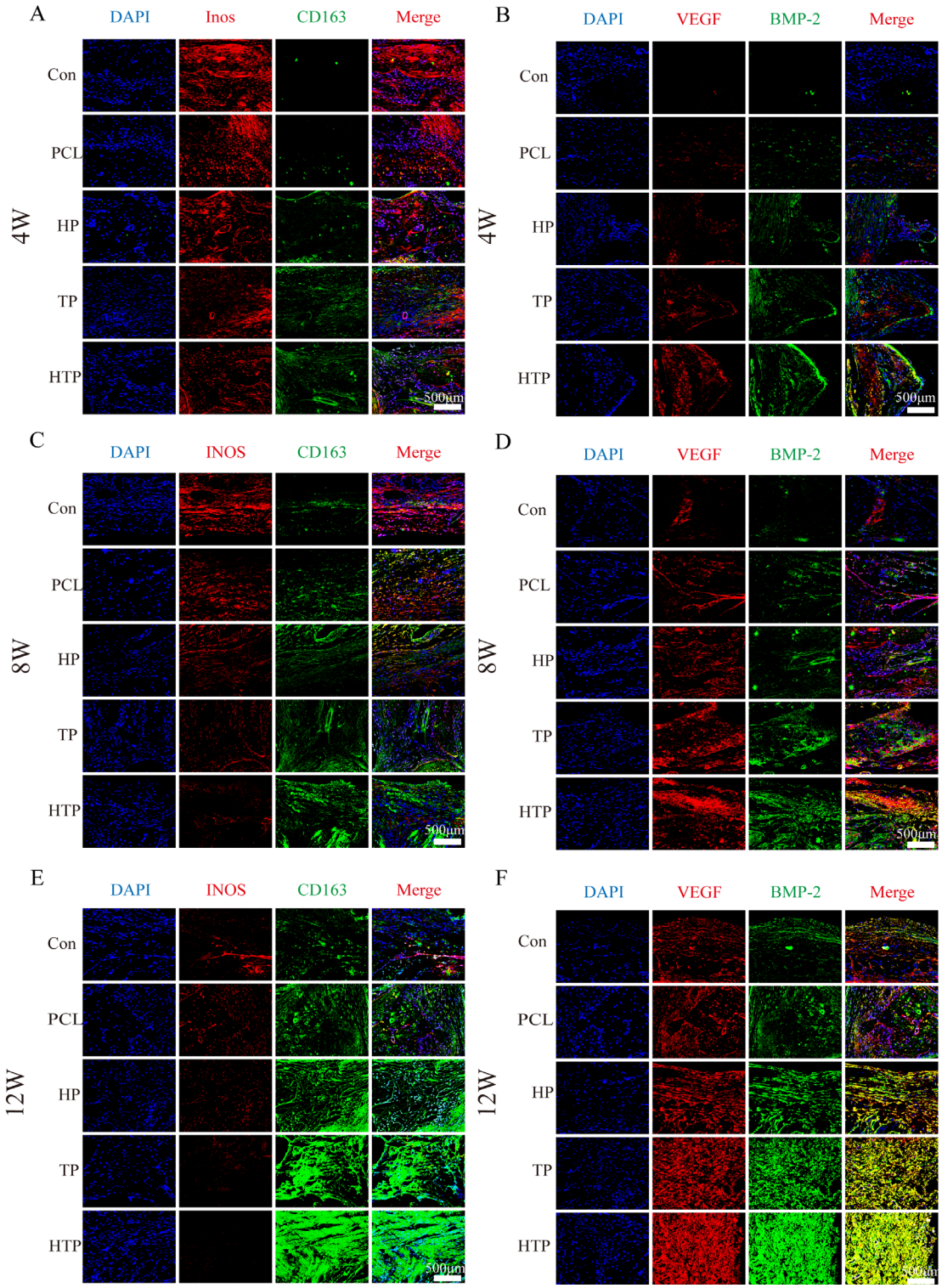

Figure 17. Triple immunofluorescence staining of rat calvarial defects at weeks (A, B) 4, (C, D) 8, and (E, F) 12 post-implantation (scale bar = 500 μm; magnification = 5×). (A, C, E) DAPI (blue) labels cell nuclei, iNOS (red) labels M1 macrophages, and CD163 (green) labels M2 macrophages. (B, D, F) DAPI (blue) labels cell nuclei, VEGF (red) labels angiogenesis, and BMP-2 (green) labels bone formation.

Abbreviations: BMP-2: Bone morphogenetic protein-2; CD163: Cluster of differentiation 163; Con: Control; DAPI: 4',6-diamidino-2-phenylindole; HP: Hydroxyapatite/polycaprolactone; HTP: Hydroxyapatite/tricalcium phosphate/polycaprolactone; iNOS: Inducible nitric oxide synthase; PCL: Polycaprolactone; TP: Tricalcium phosphate/polycaprolactone; VEGF: Vascular endothelial growth factor.

Table 3. Blood parameters of rats in each group at weeks 4, 8, and 12 post-surgery

Time point (week)	Blood parameter	Group					*p*
		Con	PCL	HP	TP	HTP	
4	WBC (×10⁹/L)	10.61 ± 1.50	11.61 ± 2.74	12.12 ± 2.58	11.20 ± 2.66	11.21 ± 2.13	0.9500
	RBC (×10⁹/L)	8.22 ± 0.48	7.70 ± 0.41	8.07 ± 0.61	7.95 ± 0.58	7.89 ± 0.51	0.7930
	HB (g/L)	132.50 ± 6.5	147.50 ± 11.02	142.00 ± 9.87	143.00 ± 11.00	142 ± 10.32	0.4900
	PLT (×10⁹/L)	1010.00 ± 102.24	950.50 ± 83.15	960.50 ± 146.79	930.00 ± 124.04	960.59 ± 120.66	0.9390
	ALT (U/L)	70.00 ± 1.42	69.00 ± 1.39	68.50 ± 3.56	69.33 ± 4.56	68.59 ± 2.69	0.9700
	AST (U/L)	110.50 ± 12.85	109.50 ± 15.68	111.00 ± 13.35	103.00 ± 10.66	110.21 ± 9.18	0.9280
	Urea (mmol/L)	6.66 ± 0.25	5.66 ± 0.59	6.78 ± 1.01	6.84 ± 0.44	6.98 ± 1.03	0.2570
	Cr (μmol/L)	45.00 ± 6.73	41.50 ± 4.54	42.50 ± 6.78	43.00 ± 3.66	42.21 ± 3.20	0.9360
8	WBC (×10⁹/L)	10.90 ± 1.41	11.80 ± 2.12	12.10 ± 1.95	11.00 ± 1.61	11.30 ± 1.52	0.8900
	RBC (×10⁹/L)	8.18 ± 0.45	7.85 ± 0.40	8.05 ± 0.55	7.92 ± 0.50	7.98 ± 0.48	0.9270
	HB (g/L)	136.5 ± 7.5	142.0 ± 10.0	140.0 ± 9.0	138.5 ± 8.8	139.0 ± 9.5	0.9580
	PLT (×10⁹/L)	995 ± 120.11	945 ± 105.15	975 ± 135.10	960 ± 125.09	980 ± 128.01	0.9890
	ALT (U/L)	69.8 ± 1.9	68.6 ± 2.2	69.2 ± 2.6	68.9 ± 2.5	69.0 ± 2.3	0.9750
	AST (U/L)	110.0 ± 13.0	106.5 ± 14.5	109.0 ± 12.5	105.5 ± 12.0	108.0 ± 13.5	0.9930
	Urea (mmol/L)	6.70 ± 0.45	6.10 ± 0.60	6.85 ± 0.75	6.55 ± 0.50	6.65 ± 0.70	0.6400
	Cr (μmol/L)	44.0 ± 5.5	41.0 ± 4.5	43.0 ± 6.0	42.0 ± 4.2	42.5 ± 4.8	0.9600
12	WBC (×10⁹/L)	10.70 ± 1.51	11.40 ± 1.92	11.60 ± 1.83	10.90 ± 1.62	11.20 ± 1.71	0.9650
	RBC (×10⁹/L)	8.10 ± 0.44	7.78 ± 0.46	8.02 ± 0.50	7.90 ± 0.47	7.95 ± 0.43	0.9280
	HB (g/L)	135.0 ± 8.0	140.5 ± 9.5	138.5 ± 9.0	137.0 ± 8.5	138.0 ± 9.2	0.9560
	PLT (×10⁹/L)	990 ± 118	940 ± 110	970 ± 130	955 ± 120	975 ± 125	0.9880
	ALT (U/L)	69.0 ± 2.0	68.2 ± 2.4	68.8 ± 2.8	68.5 ± 2.6	68.6 ± 2.5	0.9960
	AST (U/L)	109.0 ± 12.5	105.0 ± 13.0	108.0 ± 12.0	104.5 ± 11.5	107.0 ± 13.0	0.9890
	Urea (mmol/L)	6.75 ± 0.55	6.20 ± 0.65	6.90 ± 0.80	6.60 ± 0.60	6.70 ± 0.75	0.7670
	Cr (μmol/L)	43.5 ± 5.0	40.5 ± 4.2	42.8 ± 5.8	41.8 ± 4.0	42.2 ± 4.6	0.9500

Abbreviations: ALT: Alanine aminotransferase; AST: Aspartate aminotransferase; Con: Control; Cr: Creatinine; HB: Hemoglobin; HTP: Hydroxyapatite/tricalcium phosphate/polycaprolactone; TP: Tricalcium phosphate/polycaprolactone; HP: Hydroxyapatite/polycaprolactone; PCL: Polycaprolactone; PLT: Platelet; RBC: Red blood cell; WBC: White blood cell.

wt%.[28] By dividing the total ceramic content between HA and TCP, the HTP scaffold may mitigate this limitation. At the same time, it may preserve long-term structural support through the slowly resorbing HA phase, in contrast to TP scaffolds, in which the relatively rapid resorption of TCP has been reported to compromise mechanical integrity within weeks.[29]

Although the compressive modulus values reported in this study were obtained under dry conditions, the ceramic reinforcement conferred by HA and β-TCP is expected to partially compensate for hydration-induced softening of the polymer matrix *in vivo*.[30] In addition, the non-load–bearing nature of the calvarial defect model, together with the gradual biological reinforcement associated with newly formed bone ingrowth into the scaffold, likely provides sufficient mechanical support during the repair process.

Ion release profiling over three days showed that the HP scaffold produced the highest Ca^{2+} and PO_4^{3-} concentrations on day 1, whereas the TP and HTP scaffolds released comparably lower amounts at the same time point. By day 3, ion release from the HP scaffold had declined markedly, while the TP and HTP scaffolds maintained relatively stable release levels (Figure 5A and 5B). In terms of cumulative release, the overall rank order remained HP > TP > HTP throughout the observation period (Figure 5C and 5D).

The pronounced early release observed in the HP group may be attributed to the high specific surface area and

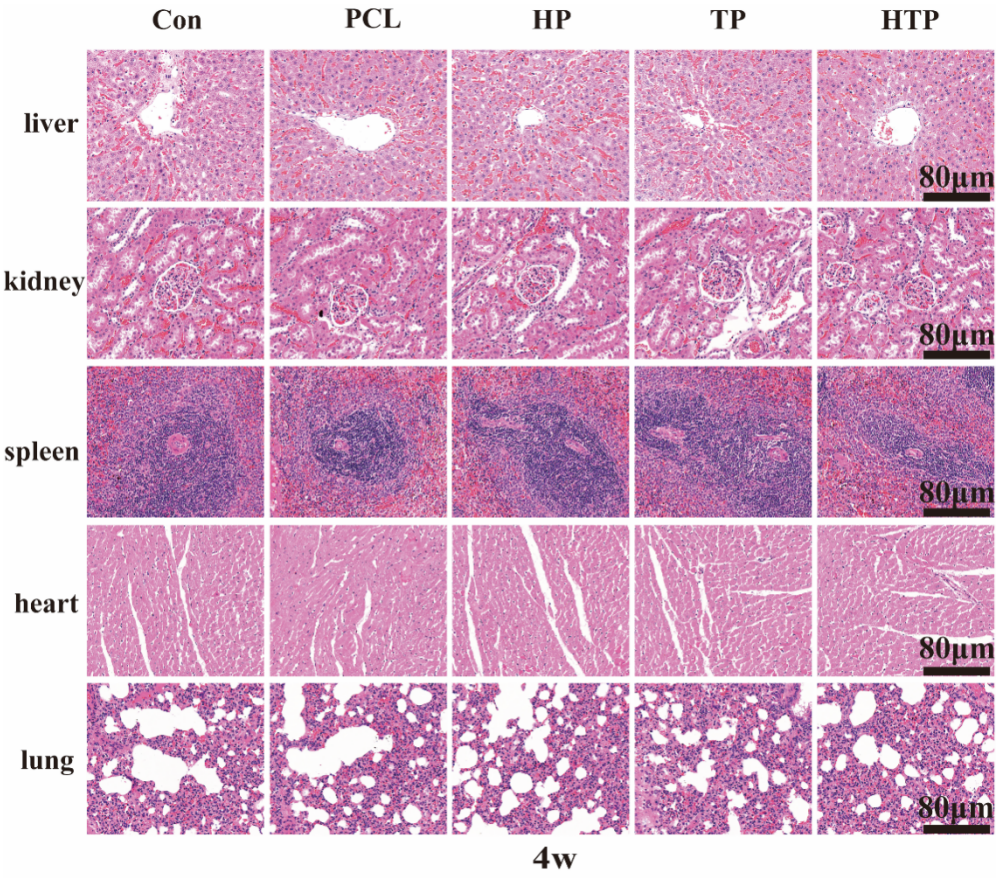

Figure 18. Hematoxylin and eosin staining of the heart, liver, spleen, lung, and kidney tissues of rats at week 4 post-operation (scale bar = 80 μm; magnification = 40×).
Abbreviations: Con: Control; HP: Hydroxyapatite/polycaprolactone; HTP: Hydroxyapatite/tricalcium phosphate/polycaprolactone; PCL: Polycaprolactone; TP: Tricalcium phosphate/polycaprolactone.

nanoscale crystal dimensions of HA particles, which can generate a transient dissolution burst upon initial contact with the aqueous environment. As the HA surface becomes progressively passivated, the release rate correspondingly decreases by day 3.[31]

The lower cumulative ion release of the HTP scaffold relative to both binary scaffolds suggests that the co-incorporation of HA and β-TCP within the PCL matrix may exert a mutual dissolution-suppressing effect, possibly through localized ionic saturation that thermodynamically limits the further dissolution of both phases.[32] Notably, the moderated and relatively sustained release profile of the HTP scaffold, rather than the highest absolute ion output, is consistent with the established view that Ca^{2+} promotes M2 macrophage polarization within an appropriate concentration range, whereas a relatively high concentration may attenuate this effect.[33] This may provide a physicochemical basis for the superior immunomodulatory performance of the HTP scaffold observed in the subsequent experiments.

The HTP scaffolds supported significantly greater BMSC adhesion and proliferation than all other groups at 24 h and 72 h (Figure 6A and 6B). This enhancement may be attributed to several factors. Increased surface roughness can expand the available sites for integrin binding, while improved wettability is more favorable for the selective adsorption of adhesion-related proteins such as fibronectin and vitronectin, which are key mediators of integrin-dependent cell attachment. In addition, Ca^{2+} released from the ceramic phases may activate integrin β1/focal adhesion kinase signaling, thereby promoting focal adhesion assembly and the cytoskeletal reorganization required for stable cell anchorage.[34]

The HP group showed better cell performance than the PCL group, likely because the incorporation of HA improved surface wettability. However, it remained inferior to the HTP group, suggesting that the combined

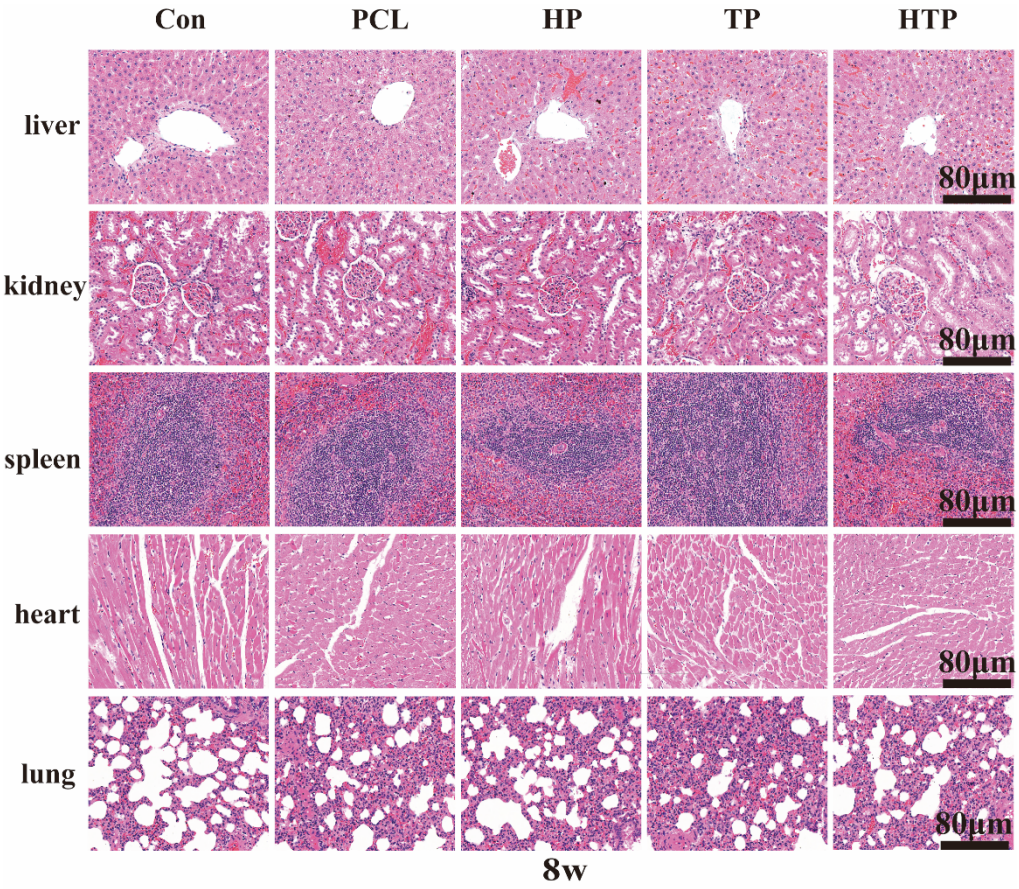

Figure 19. Hematoxylin and eosin staining of the heart, liver, spleen, lung, and kidney tissues of rats at week 8 post-operation (scale bar = 80 μm; magnification = 40×).
Abbreviations: Con: Control; HP: Hydroxyapatite/polycaprolactone; HTP: Hydroxyapatite/tricalcium phosphate/polycaprolactone; PCL: Polycaprolactone; TP: Tricalcium phosphate/polycaprolactone.

topographic and ionic contributions of HA and β-TCP, rather than a simple additive effect, played an important role in enhancing the cell response.[29]

The HTP scaffold significantly promoted the osteogenic differentiation of BMSCs, with the expression levels of osteogenic markers, including *Alp*, *Runx2*, *Opn*, *Col1a1*, and *Bmp2*, being markedly higher than those in the other groups on both days 7 and 14 (Figure 7A–7E). Under osteogenic induction conditions, ALP staining intensity and calcium deposition were most pronounced in the HTP group (Figure 8A–8D).

This enhanced osteoinductive effect may be explained by several factors. First, both HA and TCP possess intrinsic osteoconductive properties, and their composition closely resembles that of human bone mineral, thereby providing a favorable microenvironment for the osteogenic differentiation of mesenchymal stem cells even in the absence of exogenous osteogenic factors.[35] Second, the combination of HA and TCP may generate a synergistic osteogenic effect: HA provides a relatively stable osteoconductive surface for cell adhesion, whereas Ca^{2+} and PO_4^{3-} released from TCP may activate the BMP/Smad signaling pathway.

Compared with the HP scaffold previously reported[36], whose osteogenic capacity is limited by restricted ion release and insufficient sustained induction, and the TP scaffold reported elsewhere[37], whose structural support is compromised by relatively rapid degradation, the HTP scaffold appears to better balance biological activity and structural stability. This may explain why the HP group exhibited only limited osteogenesis, whereas the TP group showed a plateau in bone formation after 8 weeks, while the HTP group continued to improve throughout the observation period (Figure 13).

RAW264.7 murine macrophages were selected as the *in vitro* immunological model in the present study. Although

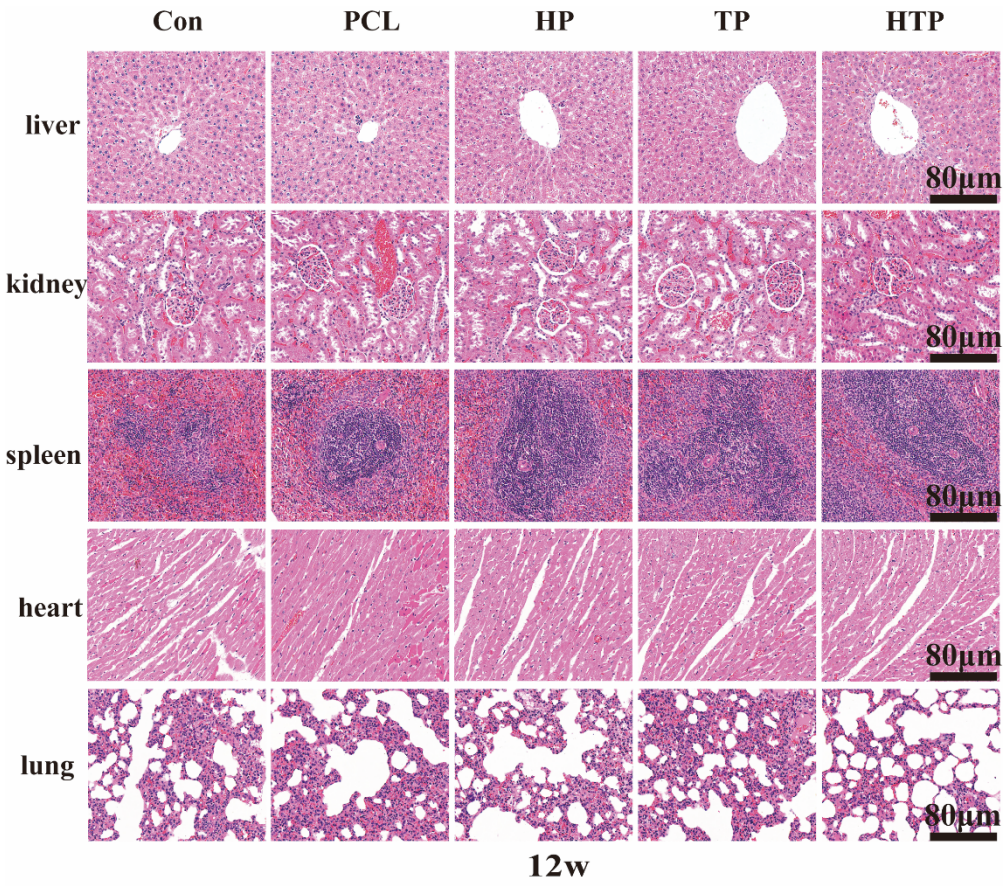

Figure 20. Hematoxylin and eosin staining of the heart, liver, spleen, lung, and kidney tissues of rats at week 12 post-operation (scale bar = 80 μm; magnification = 40×).
Abbreviations: Con: Control; HP: Hydroxyapatite/polycaprolactone; HTP: Hydroxyapatite/tricalcium phosphate/polycaprolactone; PCL: Polycaprolactone; TP: Tricalcium phosphate/polycaprolactone.

their use alongside rat BMSCs introduces a cross-species mismatch into the immune–osteogenic coupling system, RAW264.7 cells represent a widely accepted and standardized platform for bone immunology research, exhibiting conserved M1/M2 polarization signatures and cytokine secretion profiles relative to primary macrophages.[38] This standardization facilitates cross-study comparability and ensures experimental reproducibility. HTP scaffolds significantly suppressed the expression of M1-associated marker genes (*Tnfa* and *Il1b*) while upregulating the expression of M2-associated marker genes (*Mrc1* and *Arg1*) on both days 1 and 3.

In addition, ELISA showed that the HTP group produced the lowest IL-12 and the highest IL-10 concentrations in conditioned medium (Figure 9A–9F). This bidirectional immunoregulatory effect may be explained by four convergent mechanisms. First, the sustained and moderate release of Ca^{2+} may activate macrophage calcium-sensing receptor/cyclic adenosine monophosphate/protein kinase A signaling, thereby promoting IL-10 secretion through cyclic adenosine monophosphate response element-binding protein phosphorylation while attenuating nuclear factor κ-light-chain-enhancer of activated B cells–driven M1 transcription.[39] Second, improved surface hydrophilicity may reduce the non-specific adsorption of pro-inflammatory proteins such as IgG and fibrinogen, thereby limiting Fc receptor-mediated M1 activation.[40] Third, the alkaline degradation products of HA and β-TCP may partially neutralize the acidic by-products generated during PCL hydrolysis, thus preventing hypoxia-inducible factor 1α–driven M1 polarization. Fourth, the HA crystal surface may promote M2 commitment through integrin αvβ3–signal transducer and activator of transcription 6 signaling.[14]

Although Wang *et al.*[41] reported modest immunomodulatory effects in single-phase calcium phosphate materials, and Ni *et al.*[30] showed that β-TCP alone lacks sustained M2-guiding capacity, these findings

were obtained from single-phase systems and therefore do not reflect the potential mechanistic interplay between HA and β-TCP when co-incorporated within a polymer matrix. The present results suggest that biphasic ceramic co-incorporation within a polymeric matrix is important for achieving synergistic and sustained suppression of M1 polarization together with promotion of the M2 phenotype. Nevertheless, the relative contribution of each mechanism was not examined directly in the present study, and further inhibitor- or chelation-based experiments are needed to clarify their individual causal roles.

Flow cytometric analysis based on CD86/CD206 double staining further confirmed the polarization trends at the phenotypic level (Figure 10). The proportion of $CD86^{+}CD206^{-}$ (M1-like) cells decreased from 12.7% in the PCL group to 5.39% in the HTP group, whereas the proportion of $CD86^{-}CD206^{+}$ (M2-like) cells reached 24.3% in the HTP group, representing the highest level among all groups. The consistency across three independent readouts, namely M1/M2-related gene expression, cytokine secretion, and surface marker phenotype, strengthens the conclusion that the HTP scaffold exerts a genuine and sustained immunomodulatory effect rather than merely inducing a transient transcriptional response. It is noteworthy that the HP group exhibited a lower proportion of M2-like cells (15.0%) than the TP group (19.8%), which appears inconsistent with previous reports showing that HA coatings induce stronger M2 polarization than β-TCP coatings on titanium substrates.[42] This difference may be explained by the distinct material architectures involved. In coating-based systems, ion release is minimal and relatively comparable between phases, making surface chemistry the dominant factor; under such conditions, HA surfaces may be more favorable for M2 commitment.

In contrast, in the present composite system, the HP scaffold released substantially higher levels of Ca^{2+} and PO_4^{3-} on day 1 (Figure 5). Given that Ca^{2+} promotes M2 polarization only within an appropriate concentration range, whereas excessively high concentrations may induce a mixed M1/M2 phenotype[43], the early ionic burst observed in the HP group may have weakened the overall M2-promoting effect. By comparison, the lower-amplitude ion release of the TP group may have remained within a more favorable pro-M2 range. This interpretation is consistent with previous evidence indicating that sustained and moderate Ca^{2+} delivery, rather than peak concentration, is a key determinant of M2 polarization through calcium-sensing receptor–Wnt/β-catenin signaling.[39] Further dose–response experiments specifically designed to define the relationship between Ca^{2+} concentration and macrophage polarization are needed to verify this interpretation directly.

Moreover, BMSCs cultured in HTP-conditioned medium expressed significantly higher levels of *Alp*, *Runx2*, *Bmp2*, *Col1a1*, and *Opn* than those cultured in conditioned medium from the other groups or under direct exogenous osteogenic induction on both days 7 and 14 (Figure 11). Under immuno-osteogenic conditions, the HTP group also showed the highest ALP staining intensity and calcium deposition, reaching approximately two-fold higher levels than the next best group, as determined by semi-quantitative analysis (Figure 12A–12D). These findings indicate that the immunological microenvironment generated by HTP is itself osteoinductive, even in the absence of direct scaffold–cell contact. This effect may be mediated by three major paracrine signals associated with M2 macrophages. Transforming growth factor-β1 can activate Smad2/3 signaling and promote *Runx2* upregulation[44]; BMP-2 can further enhance osteoprogenitor commitment through Smad1/5/8 phosphorylation; and the elevated IL-10 level in HTP-conditioned medium may relieve nuclear factor κ-light-chain-enhancer of activated B cells–mediated suppression of BMP receptor expression, thereby collectively strengthening the osteogenic response beyond that achieved by conventional dexamethasone-based induction alone.[45]

The temporal pattern of gene expression was also consistent with a staged osteogenic process: *Runx2* and *Alp* were more prominently expressed on day 7, suggesting early osteoprogenitor commitment driven by the M2-associated microenvironment, whereas *Bmp2*, *Col1a1*, and *Opn* were more pronounced on day 14, reflecting continued matrix synthesis and maturation. Across all ceramic-containing groups, mineralization under immuno-osteogenic conditions exceeded that observed in the direct osteogenesis model, indicating that macrophage-conditioned medium provided an additional pro-mineralization stimulus. Although previous studies have shown that the M2-derived secretome can promote BMSC mineralization in isolated systems[46], those studies did not involve a defined material platform. In contrast, the present results directly associate a specific scaffold composition with enhanced paracrine osteogenesis, providing mechanistic support for the concept that material-directed macrophage polarization may serve as an effective strategy to promote bone regeneration.

The HTP scaffold significantly promoted new bone formation in the rat calvarial defect model, showing the highest BV/TV and BMD values at all time points (Figures 13 and 14). Histological examination revealed that the Con and PCL groups were predominantly filled with fibrous tissue, whereas only scattered woven bone was observed

in the HP and TP groups. In contrast, the HTP group exhibited a continuous lamellar bone structure, with newly formed bone trabeculae closely integrated with the host bone (Figures 15 and 16). This superior *in vivo* performance may be associated with the coupling axis among immune regulation, angiogenesis, and osteogenesis. Kusumbe *et al.*[47] identified H-type vessels ($CD31^{hi}Emcn^{hi}$) that directly couple angiogenesis with osteogenesis, with osteoprogenitor cells enriched around these vessels. Liu *et al.*[48] further demonstrated that a reduction in H-type vessels is accompanied by decreased osteogenic capacity. Huang *et al.*[21] reported that macrophages serve as a key endogenous source of VEGF, and that timely conversion from the M1 to the M2 phenotype facilitates the coordinated interaction between angiogenesis and osteogenesis. The immunofluorescence results of the present study support this framework: the M2/M1 ratio in the HTP group was significantly higher than that in the other groups, with M2 macrophages becoming predominant by week 12, whereas the control and P groups remained in a predominantly M1-driven pro-inflammatory state (Figure 17A, 17C, and 17E).

The spatial co-localization of VEGF and BMP-2 within the defect area of the HTP group provided direct evidence of immune–vascular–osteogenesis coupling (Figure 17B, 17D, and 17F). At week 4 postoperatively, a distinct VEGF-positive neovascular network accompanied by BMP-2–positive signals was observed. By week 12, both signals were further enhanced and showed a high degree of overlap. This triaxial mechanism may operate through a positive feedback loop in which M2 macrophages secrete VEGF to promote angiogenesis, thereby facilitating nutrient supply and stem cell recruitment, while BMP-2 simultaneously promotes the osteogenic differentiation of BMSCs. Newly formed blood vessels may further enhance the recruitment of MSCs and growth factors, thereby accelerating the bone regeneration process. This may represent a key distinction between the HTP scaffold and traditional passive osteoconductive materials, which primarily rely on structural support without active immunomodulatory regulation.

The immunomodulatory effects of the HTP scaffold were achieved entirely through material composition, without the incorporation of exogenous growth factors or cytokines. This distinguishes it from cytokine-loading strategies, such as those based on IL-4 or IL-10, reported by Zhang *et al.*[49], which are often limited by protein instability, uncontrolled release kinetics, manufacturing cost, and potential immunogenicity. In contrast, the intrinsic physicochemical cues of the HTP scaffold, including ion release kinetics, surface microtopography, and pH-buffering capacity, are determined by the material architecture itself and are therefore, in principle, more reproducible than protein-based release profiles. Moreover, all three constituent materials have received regulatory approval for orthopedic applications, and systemic toxicological evaluation in the present study revealed no evident hematological, hepatic, renal, or histopathological abnormalities (Table 3, Figures 18–20), suggesting that their combination did not generate harmful metabolic by-products. Collectively, the current findings support the potential application of the HTP scaffold in craniofacial non-load–bearing defects, although its translation to load-bearing sites will require further validation in large-animal models with mechanical assessment.

Several limitations of the present study should be acknowledged. From the perspective of experimental design, the 12-week observation period captured only the early and intermediate phases of repair, leaving long-term scaffold degradation and bone remodeling insufficiently characterized. In addition, because the rat calvarial defect model is non-load–bearing, the performance of the scaffold in load-bearing applications cannot be inferred from the present data, and biomechanical validation in large-animal models will be required before clinical translation. The use of murine RAW264.7 macrophages together with rat BMSCs introduced a cross-species mismatch into the *in vitro* immune–osteogenic coupling model. Although RAW264.7 cells are a widely accepted standardized model for bone immunology research and exhibit conserved M1/M2 polarization signatures relative to primary macrophages[38], their inflammatory threshold and cytokine profiles may differ quantitatively from those of rat BMDMs. Future studies should reproduce the key polarization and conditioned-medium osteogenesis experiments in rat BMDMs to improve biological relevance.

5. Conclusion

This study developed a 3D-printed HTP composite scaffold as a bone immune modulation platform for regulating the local immune microenvironment and promoting bone regeneration. The HTP scaffold not only serves as structural support but also actively guides macrophage polarization toward the regenerative M2 phenotype, combining immune modulation with osteogenesis and angiogenesis. Notably, the synergistic effect of HA and TCP endows this scaffold with stronger immune modulation and osteogenic performance than pure PCL and single ceramic-modified scaffolds (HP and TP), highlighting the importance of component synergy in scaffold design. This immune-mediated regulation further promotes vascularized bone formation and accelerates calvarial defect repair. Overall, these findings emphasize the potential of the 3D-printed

HTP composite scaffold as a promising bone tissue engineering immune-modulating strategy and provide design principles for developing next-generation immune-regulating biomaterials for complex bone defect repair.

Acknowledgments

None

Funding

This study was supported by the National Natural Science Foundation of China (32571583), the Guangdong Province Science and Technology Plan Project (2024A1515012265), the Zunyi City Science and Technology Innovation Talent Project (No. [2024] 04), and the GDAS Project of Science and Technology Development (2023GDASZH-2023010102).

Conflict of interest

The authors declare that they have no known competing financial interests or personal relationships that could have appeared to influence the work reported in this paper.

Author contributions

Conceptualization: Jiaxiang Song, Qingde Wa
Data curation: Qianyu Xie
Formal analysis: Guangquan Zhao
Funding acquisition: Weikang Xu, Qingde Wa
Investigation: Hao Tang
Methodology: Hao Tang, Guangquan Zhao, Yuanhao Lv
Resources: Guangquan Zhao
Software: Hao Tang, Yuanhao Lv
Supervision: Weikang Xu, Qingde Wa
Validation: Hao Tang, Yuanhao Lv
Visualization: Qianyu Xie, Jiaxiang Song
Writing–original draft: Hao Tang
Writing–review & editing: Weikang Xu, Qingde Wa

Ethics approval and consent to participate

The animal experimental protocol in this study was approved by the Animal Welfare Committee of Zunyi Medical University (Approval No. ZMUAEC-2603-145). All procedures were conducted in strict accordance with relevant national laws and regulations, as well as the ethical principles for laboratory animal welfare, to ensure the health and well-being of the animals.

Consent for publication

Not applicable.

Availability of data

All data generated or analyzed during this study are included in this published article.

References

1. Ma XY, Yuan H, Cui D, *et al*. Management of segmental defects post open distal femur fracture using a titanium cage combined with the masquelet technique a single-centre report of 23 cases. *Injury*. 2023;54(12):111130.

   doi: 10.1016/j.injury.2023.111130

2. Zheng S, Zhong H, Cheng H, *et al*. Engineering multifunctional hydrogel with osteogenic capacity for critical-size segmental bone defect repair. *Front Bioeng Biotechnol*. 2022;10:899457.

   doi: 10.3389/fbioe.2022.899457

3. Engel EE, Gava NF, Santos MA dos, Baldoino LG, Ismael LK, Modolo LFM. Updates on bone grafts and substitutes. *Rev Bras Ortop*. 2025;60(6):s00451814114.

   doi: 10.1055/s-0045-1814114

4. Ferraz MP. Bone grafts in dental medicine: An overview of autografts, allografts and synthetic materials. *Materials*. 2023;16(11):4117.

   doi: 10.3390/ma16114117

5. Ciszyński M, Dominiak S, Dominiak M, Gedrange T, Hadzik J. Allogenic bone graft in dentistry: A review of current trends and developments. *Int J Mol Sci*. 2023;24(23):16598.

   doi: 10.3390/ijms242316598

6. Wang H, Kang J. Bone grafts and synthetic substitutes in dental applications: A comprehensive review of molecular mechanisms, materials evolution, and clinical perspective. *Front Bioeng Biotechnol*. 2026;13:1759864.

   doi: 10.3389/fbioe.2025.1759864

7. Gharibshahian M, Salehi M, Beheshtizadeh N, *et al*. Recent advances on 3D-printed PCL-based composite scaffolds for bone tissue engineering. *Front Bioeng Biotechnol*. 2023;11:1168504.

   doi: 10.3389/fbioe.2023.1168504

8. Sun J, Chen C, Zhang B, Yao C, Zhang Y. Advances in 3D-printed scaffold technologies for bone defect repair: Materials, biomechanics, and clinical prospects. *Biomed Eng Online*. 2025;24:51.

   doi: 10.1186/s12938-025-01381-w

9. Bellen F, Carbone E, Baatsen P, Jones EAV, Kabirian F, Heying R. Improvement of endothelial cell-polycaprolactone interaction through surface modification via aminolysis, hydrolysis, and a combined approach. *J Tissue Eng Regener Med*. 2023;2023:5590725.

   doi: 10.1155/2023/5590725

10. Farjaminejad S, Farjaminejad R, Hasani M, *et al*. Advances and challenges in polymer-based scaffolds for bone tissue engineering: a path towards personalized regenerative medicine. *Polymers*. 2024;16(23):3303.

doi: 10.3390/polym16233303

11. Ielo I, Calabrese G, De Luca G, Conoci S. Recent advances in hydroxyapatite-based biocomposites for bone tissue regeneration in orthopedics. *Int J Mol Sci*. 2022;23(17):9721.

doi: 10.3390/ijms23179721

12. Ye X, Zhang Y, Liu T, *et al*. Beta-tricalcium phosphate enhanced mechanical and biological properties of 3D-printed polyhydroxyalkanoates scaffold for bone tissue engineering. *Int J Biol Macromol*. 2022;209:1553-1561.

doi: 10.1016/j.ijbiomac.2022.04.056

13. Ramanathan M, Shijirbold A, Okui T, *et al*. In vivo evaluation of bone regenerative capacity of the novel nanobiomaterial: β-tricalcium phosphate polylactic acid-co-glycolide (β-TCP/PLLA/PGA) for use in maxillofacial bone defects. *Nanomaterials*. 2023;14(1):91.

doi: 10.3390/nano14010091

14. Wu H, Wei X, Liu Y, *et al*. Dynamic degradation patterns of porous polycaprolactone/β-tricalcium phosphate composites orchestrate macrophage responses and immunoregulatory bone regeneration. *Bioact Mater*. 2022;21:595-611.

doi: 10.1016/j.bioactmat.2022.07.032

15. Ruckh TT, Carroll DA, Weaver JR, Popat KC. Mineralization content alters osteogenic responses of bone marrow stromal cells on hydroxyapatite/polycaprolactone composite nanofiber scaffolds. *J Funct Biomater*. 2012;3(4):776-798.

doi: 10.3390/jfb3040776

16. Ghezzi B, Matera B, Meglioli M, *et al*. Composite PCL scaffold with 70% β-TCP as suitable structure for bone replacement. *Int Dent J*. 2024;74(6):1220-1232.

doi: 10.1016/j.identj.2024.02.013

17. Guder C, Gravius S, Burger C, Wirtz DC, Schildberg FA. Osteoimmunology: A current update of the interplay between bone and the immune system. *Front Immunol*. 2020;11:58.

doi: 10.3389/fimmu.2020.00058

18. Batool F, Özçelik H, Stutz C, *et al*. Modulation of immune-inflammatory responses through surface modifications of biomaterials to promote bone healing and regeneration. *J Tissue Eng*. 2021;12:20417314211041428.

doi: 10.1177/20417314211041428

19. Wang J, Yuan B, Yin R, Zhang H. Inflammation responses to bone scaffolds under mechanical stimuli in bone regeneration. *J Funct Biomater*. 2023;14(3):169.

doi: 10.3390/jfb14030169

20. Wang Y, Wang B, Liu D, *et al*. Osteoimmunology uncovered: How macrophages and biomaterials revolutionize bone healing. *Mater Today Bio*. 2026;36:102647.

doi: 10.1016/j.mtbio.2025.102647

21. Huang S, Zeng A, Yin Q, *et al*. Progress in immunoregulatory mechanisms during distraction osteogenesis. *Front Bioeng Biotechnol*. 2025;13:1665192.

doi: 10.3389/fbioe.2025.1665192

22. Liu W, Cheong N, He Z, Zhang T. Application of hydroxyapatite composites in bone tissue engineering: A review. *J Funct Biomater*. 2025;16(4):127.

doi: 10.3390/jfb16040127

23. Yao H, Zhu W, Zhu X, *et al*. Development of hydroxyapatite/polycaprolactone composite biomaterials for laser powder bed fusion: Evaluation of powder characteristics, mechanical properties and biocompatibility. *Polymers*. 2024;16(6):731.

doi: 10.3390/polym16060731

24. Vajgel A, Mardas N, Farias BC, Petrie A, Cimões R, Donos N. A systematic review on the critical size defect model. *Clin Oral Implants Res*. 2014;25(8):879-893.

doi: 10.1111/clr.12194

25. Qi H, Zhang B, Lian F. 3D-printed bioceramic scaffolds for bone defect repair: Bone aging and immune regulation. *Front Bioeng Biotechnol*. 2025;13:1557203.

doi: 10.3389/fbioe.2025.1557203

26. Yuqiang W, Ziyan Z, Xuedi S, Chengdong P. Recent progress in immunomodulation-based strategies for bone repair. *Regen Ther*. 2025;31:101054.

doi: 10.1016/j.reth.2025.101054

27. Chen M, Chen Y, He H, Zhou X, Chen N. Structure and property evolution of microinjection molded PLA/PCL/bioactive glass composite. *Polymers*. 2025;17(7):991.

doi: 10.3390/polym17070991

28. Li Y, Yu Z, Ai F, *et al*. Characterization and evaluation of polycaprolactone/hydroxyapatite composite scaffolds with extra surface morphology by cryogenic printing for bone tissue engineering. *Mater Des*. 2021;205:109712.

doi: 10.1016/j.matdes.2021.109712

29. Helaehil JV, Lourenço CB, Huang B, *et al*. In vivo investigation of polymer-ceramic PCL/HA and PCL/β-TCP 3D composite scaffolds and electrical stimulation for bone regeneration. *Polymers*. 2021;14(1):65.

doi: 10.3390/polym14010065

30. Ni X, Feng J, Liang M, *et al*. Enhancing bone repair with β-TCP-based composite scaffolds: A review of design strategies and biological mechanisms. *Orthop Res Rev*. 2025;17:313-340.

doi: 10.2147/ORR.S525959

31. Ardeshiriansharifabadi S, Asefnejad A, Azami M. 3D-printed polycaprolactone/nano-hydroxyapatite scaffold coated by zein for controlled release of tetracycline hydrochloride in

bone tissue engineering. *Results Eng*. 2026;29:109540.

doi: 10.1016/j.rineng.2026.109540

32. Thuaksuban N, Monmaturapoj N, Luntheng T. Effects of polycaprolactone-biphasic calcium phosphate scaffolds on enhancing growth and differentiation of osteoblasts. *Biomed Mater Eng*. 2018;29(2):159-176.

doi: 10.3233/BME-171720

33. Pogonyalova MY, Popov DY, Vinokurov AY. Intracellular calcium as a regulator of polarization and target reprogramming of macrophages. *Int J Mol Sci*. 2025;26(24):11901.

doi: 10.3390/ijms262411901

34. Tollabi M, Poursalehi Z, Mehrafshar P, *et al*. Insight into the role of integrins and integrins-targeting biomaterials in bone regeneration. *Connect Tissue Res*. 2024;65(5):343-363.

doi: 10.1080/03008207.2024.2396002

35. Polini A, Pisignano D, Parodi M, Quarto R, Scaglione S. Osteoinduction of human mesenchymal stem cells by bioactive composite scaffolds without supplemental osteogenic growth factors. *PLoS ONE*. 2011;6(10):e26211.

doi: 10.1371/journal.pone.0026211

36. Gou Y, Qi K, Wei Y, Gu Z, Xie H. Advances of calcium phosphate nanoceramics for the osteoinductive potential and mechanistic pathways in maxillofacial bone defect repair. *Nano TransMed*. 2024;3:100033.

doi: 10.1016/j.ntm.2024.100033

37. Liang HY, Lee WK, Hsu JT, *et al*. Polycaprolactone in bone tissue engineering: A comprehensive review of innovations in scaffold fabrication and surface modifications. *J Funct Biomater*. 2024;15(9):243.

doi: 10.3390/jfb15090243

38. Kong L, Smith W, Hao D. Overview of RAW264.7 for osteoclastogensis study: phenotype and stimuli. *J Cell Mol Med*. 2019;23(5):3077-3087.

doi: 10.1111/jcmm.14277

39. Zhang J, Wu Q, Yin C, *et al*. Sustained calcium ion release from bioceramics promotes CaSR-mediated M2 macrophage polarization for osteoinduction. *J Leukocyte Biol*. 2021;110(3):485-496.

doi: 10.1002/JLB.3MA0321-739R

40. Lv L, Xie Y, Li K, *et al*. Unveiling the mechanism of surface hydrophilicity-modulated macrophage polarization. *Adv Healthcare Mater*. 2018;7(19):1800675.

doi: 10.1002/adhm.201800675

41. Wang M, Chen F, Tang Y, *et al*. Regulation of macrophage polarization and functional status by modulating hydroxyapatite ceramic micro/nano-topography. *Mater Des*. 2022;213:110302.

doi: 10.1016/j.matdes.2021.110302

42. Zhang Y, Cheng X, Jansen JA, Yang F, van den Beucken JJJP. Titanium surfaces characteristics modulate macrophage polarization. *Mater Sci Eng C*. 2019;95:143-151.

doi: 10.1016/j.msec.2018.10.065

43. Nascimento Da Conceicao V, Sun Y, Ramachandran K, *et al*. Resolving macrophage polarization through distinct Ca2+ entry channel that maintains intracellular signaling and mitochondrial bioenergetics. *iScience*. 2021;24(11):103339.

doi: 10.1016/j.isci.2021.103339

44. Hu L, Chen W, Qian A, Li YP. Wnt/β-catenin signaling components and mechanisms in bone formation, homeostasis, and disease. *Bone Res*. 2024;12(1):39.

doi: 10.1038/s41413-024-00342-8

45. Chen E, Liu G, Zhou X, *et al*. Concentration-dependent, dual roles of IL-10 in the osteogenesis of human BMSCs via P38/MAPK and NF-κB signaling pathways. *FASEB J*. 2018;32(9):4917-4929.

doi: 10.1096/fj.201701256RRR

46. Liu K, Luo X, Lv ZY, *et al*. Macrophage-derived exosomes promote bone mesenchymal stem cells towards osteoblastic fate through microRNA-21a-5p. *Front Bioeng Biotechnol*. 2022;9:801432.

doi: 10.3389/fbioe.2021.801432

47. Kusumbe AP, Ramasamy SK, Adams RH. Coupling of angiogenesis and osteogenesis by a specific vessel subtype in bone. *Nature*. 2014;507(7492):323-328.

doi: 10.1038/nature13145

48. Liu X, Zhang P, Gu Y, Guo Q, Liu Y. Type H vessels: Functions in bone development and diseases. *Front Cell Dev Biol*. 2023;11:1236545.

doi: 10.3389/fcell.2023.1236545

49. Zhang J, Shi H, Zhang N, Hu L, Jing W, Pan J. Interleukin-4-loaded hydrogel scaffold regulates macrophages polarization to promote bone mesenchymal stem cells osteogenic differentiation via TGF-β1/smad pathway for repair of bone defect. *Cell Prolif*. 2020;53(10):e12907.

doi: 10.1111/cpr.12907